

---


Electronic Theses and Dissertations, 2004-2019

---

2011

## Optimal Attitude Control Management For A Cubesat

Michael James Develle  
*University of Central Florida*

 Part of the [Space Vehicles Commons](#)  
Find similar works at: <https://stars.library.ucf.edu/etd>  
University of Central Florida Libraries <http://library.ucf.edu>

This Masters Thesis (Open Access) is brought to you for free and open access by STARS. It has been accepted for inclusion in Electronic Theses and Dissertations, 2004-2019 by an authorized administrator of STARS. For more information, please contact [STARS@ucf.edu](mailto:STARS@ucf.edu).

---

### STARS Citation

Develle, Michael James, "Optimal Attitude Control Management For A Cubesat" (2011). *Electronic Theses and Dissertations, 2004-2019*. 1839.  
<https://stars.library.ucf.edu/etd/1839>

OPTIMAL ATTITUDE  
CONTROL MANAGEMENT  
FOR A CUBESAT

by

MICHAEL JAMES DEVELLE II  
B.S. United States Air Force Academy, 1998

A thesis submitted in partial fulfillment of the requirements  
for the degree of Master of Science  
in the Department of Materials, Mechanical and Aerospace Engineering  
in the College of Engineering and Computer Science  
at the University of Central Florida  
Orlando, Florida

Fall Term  
2011

## **ABSTRACT**

CubeSats have become popular among universities, research organizations, and government agencies due to their low cost, small size, and light weight. Their standardized configurations further reduce the development time and ensure more frequent launch opportunities. Early cubesat missions focused on hardware validation and simple communication missions, with little requirement for pointing accuracy. Most of these used magnetic torque rods or coils for attitude stabilization. However, the intrinsic problems associated with magnetic torque systems, such as the lack of three-axis control and low pointing accuracy, make them unsuitable for more advanced missions such as detailed imaging and on-orbit inspection. Three-axis control in a cubesat can be achieved by combining magnetic torque coils with other devices such as thrusters, but the lifetime is limited by the fuel source onboard. To maximize the mission lifetime, a fast attitude control management algorithm that could optimally manage the usage of the magnetic and thruster torques is desirable. Therefore, a recently developed method, the B-Spline-augmented virtual motion camouflage, is presented in this defense to solve the problem. This approach provides results which are very close to those obtained through other popular nonlinear constrained optimal control methods with a significantly reduced computational time. Simulation results are presented to validate the capabilities of the method in this application.

Dedicated to my grandfather, who inspired this journey.

## ACKNOWLEDGMENTS

This thesis was made possible by the talents and the generosity of many others. Although I will try, I know that I cannot list everyone that is deserving of thanks. I am grateful to God first, for giving me the ability to complete this project and for the people He sent to help me. People like my parents, who sacrificed so I could attend good schools to give me the foundation I needed. Thank you to my grandparents - for listening to me, encouraging me and inspiring me to do more. Thank you to everyone at UCF who supported me. My committee members - Dr. Kuo-Chi Lin and Dr. Larry Chew - gave their time and advice to make this thesis possible. Gareth, Ni, Brad, Forhad, Puneet and Charles offered suggestions when I was stuck, kept me smiling and allowed me to be a part of their group. Thank you to my advisor, Dr. Xu, for numerous edits and explanations, for teaching me and for pushing me to finish.

Thank to my extended family in Wichita. My debt to you can never be repaid. You opened your home to me, prayed with me, listened to my struggles, and even cooked me dinner so I could keep working on this thesis. You taught me about love and a few important things about Astrodynamics (Eddie). To Eddie, Tonie and the girls - you are some of the finest representatives of our Lord that I have ever met.

Thank you to my son, Jimmy. He gave up time with Dad on many occasions so I could complete this project. Most importantly, thank you to my wife and my best friend, Betsy. You believed in me when no one else did, and gave up hours and days of your life to support me in this endeavor. You gave me your encouragement, your strength and your love. Thank you for bearing the weight of this project on your shoulders. For this and so many other things, I am forever indebted to you.

## TABLE OF CONTENTS

LIST OF FIGURES .....	vi
LIST OF TABLES .....	viii
LIST OF NOMENCLATURE .....	ix
CHAPTER 1: INTRODUCTION .....	1
CHAPTER 2: DYNAMICS MODEL.....	7
Coordinate Frames .....	8
Magnetic Field Model.....	11
Dimensionless Models.....	13
CHAPTER 3: VIRTUAL MOTION CAMOUFLAGE .....	14
CHAPTER 4: MINIMIZING THE TOTAL TORQUE.....	16
Problem Definition .....	16
Necessary Conditions .....	16
Generating Prey Motion and Path Control Parameters.....	18
Application - Minimize Total Torque.....	19
Simulation Scenario And Discussion .....	20
CHAPTER 5: ATTITUDE CONTROL MANAGEMENT.....	26
Problem Definition .....	26
Generating Prey Motion and Path Control Parameters.....	26
Application.....	28
Simulation Results and Discussion.....	30
CHAPTER 6: SUMMARY AND FUTURE WORK .....	43
LIST OF REFERENCES .....	45

## LIST OF FIGURES

Figure 1. Geocentric Equatorial Coordinate Frame.....	9
Figure 2. North, East, Down Coordinate Frame. ....	9
Figure 3. LVLH Coordinate Frame. ....	10
Figure 4. Rotations about the Spacecraft Body Coordinate Frame. ....	10
Figure 5. Magnetic coil interaction with magnetic field. Current is in red and flows around the coil in the magnetic field.....	12
Figure 6. Performance error between the Baseline and VMC with polynomial prey motion. ....	22
Figure 7. Quaternion of the near optimal attitude trajectory. ....	23
Figure 8. Angular velocity of the near optimal attitude trajectory. ....	24
Figure 9. VMC control torque for near optimal rotation. ....	24
Table 2. Boundary Conditions used to evaluate solutions for problem 2.....	31
Figure 10. B-Spline curve with path constraints that do not interfere with a straight line between end points.....	33
Figure 11. B-Spline curve with a path constraint that drives requirement for at least one additional control point. ....	33
Figure 12. B-Spline curve with two path constraints which drive a requirement for at least four control points. ....	34
Figure 13. Quaternion of the near optimal attitude trajectory (Case 1).....	37
Figure 14. Angular velocity of the near optimal attitude trajectory. ....	38

Figure 15. Current for near optimal rotation.....	38
Figure 16. VMC control torque for near optimal rotation (X axis). .....	39
Figure 17. VMC control torque for near optimal rotation (Y axis). .....	39
Figure 18. VMC control torque for near optimal rotation (Z axis).....	39
Figure 19. Quaternion for Case 2, B-Spline prey motion, 10 LGL Nodes, $t_f=400s$ . .....	40
Figure 20. Angular velocity for Case 2, B-Spline prey motion, 10 LGL Nodes, $t_f=400s$ . .....	40
Figure 21. Current for Case 2, B-Spline prey motion, 10 LGL Nodes, $t_f=400s$ . .....	41
Figure 22. Torque (x-axis) for Case 2, B-Spline prey motion, 10 LGL Nodes, $t_f=400s$ . .....	41
Figure 23. Torque (y-axis) for Case 2, B-Spline prey motion, 10 LGL Nodes, $t_f=400s$ . .....	42
Figure 24. Torque (z-axis) for Case 2, B-Spline prey motion, 10 LGL Nodes, $t_f=400s$ . .....	42



## LIST OF TABLES

Table 1. Total torque problem, results comparison (Polynomial prey motion).....	23
Table 2. Boundary Conditions used to evaluate solutions for problem 2. ....	31
Table 3. Comparison of B-Spline, VMC with B-Spline Prey Motion and Baseline Approaches (Case 1). ....	36
Table 4. Comparison of B-Spline, VMC with B-Spline Prey Motion and Baseline Approaches (Case 2). ....	36

## LIST OF NOMENCLATURE

- $q$  = Quaternion
- $\omega$  = Body Rates
- $q_a$  = Quaternion, aggressor motion
- $q_p$  = Quaternion, prey motion
- $q_r$  = Quaternion, reference point
- $v$  = Path control parameter
- $T$  = Total torque
- $T_c$  = Torque from magnetic torque coils
- $T_t$  = Torque from thrusters
- $a$  = Semi major axis
- $e$  = Eccentricity
- $i_n$  = Inclination
- $\Omega$  = Right ascension of the ascending node
- $\omega_{aop}$  = Argument of perigee

## **CHAPTER 1: INTRODUCTION**

CubeSats are small satellites with a mass no greater than 1.33 kg, and a 10 cm cube structure [1]. They are used primarily for education, basic research, and technology demonstration /validation. Accordingly, most CubeSats have been built by universities, with a small number built by government agencies and private companies. Since 2003, over 40 CubeSats have been launched [2]. Of those launched so far, twenty had an active attitude determination and control system (ADCS) [2-8], among which eighteen were based solely on magnetic torques. The remaining two, CANX-2 and AAUSAT-II, featured an ADCS based on a combination of magnetic torque and other systems [9-10]. Future launch plans indicate that several spacecraft in the next generation of CubeSats will have active magnetic attitude control systems - one solely based on magnetic torque [42] and at least one that is planned to use magnetic control with in addition to reaction wheels [1, 2, 3, 11].

It is clear that magnetic torque systems have been, and will continue to be, popular with CubeSat designers. CubeSats have very limited mass and volume budgets, and magnetic torque systems are cheaper and lighter than the alternatives, which include momentum wheels, reaction wheels and thrusters. In particular, when compared to thrusters, magnetic torque systems have a fuel supply (power from solar panels) that lasts for the lifetime of the satellite, where thrusters are limited to the fuel they are launched with. Despite their popularity, magnetic torque systems have important limitations. Since magnetic torque can only be produced in an axis perpendicular to the Earth's magnetic field, control is limited to two axes at any given time. Some designers have taken advantage of variations in the magnetic field seen by the spacecraft as it travels through its orbit, allowing stabilization of a spacecraft using just a magnetic torque system. This

method was pioneered by Martel and Psiaki [12]. Their proposal for a gravity gradient stabilized satellite used linearized equations of motion and a proportional derivative control law to determine the desired control torque vector. In simulations, their method stabilized the satellite within  $\pm 5$  deg of a nadir pointing attitude but took in excess of 500 seconds to complete the maneuver. Musser and Ward made the next contribution to the field [13]. To stabilize a spacecraft in a nadir pointing attitude, they used a Linear Quadratic Regulator (LQR) and solved the Riccati equation to determine the time varying feedback gain matrix. In simulation, the method stabilized the spacecraft to within  $\pm 5$  deg of a nadir pointing reference point. It was also slow, taking over 4000 seconds to complete the maneuver. For the Orsted satellite, Bak, Wisniewski and Blanke proposed a linear quadratic controller [14]. Lyapunov theory was applied, which showed that energy was dissipated by the B dot de-tumbling control law. In simulation, The B dot control law resulted in Euler angles that converged to  $\pm 10$  deg after approximately 3 orbits. These methods were further refined by Wisniewski in [15] and [16] when a locally stabilizing controller was proposed, and extended to be a globally stable time varying controller. In simulation based on the Orsted spacecraft in a low eccentricity and high inclination orbit, the spacecraft was stabilized in the operational range within 6 orbits [16]. Makovec took the methods developed by Musser and Wisniewski and optimized the gains of a constant coefficient linear quadratic regulator [17]. Simulation results showed that the controller was able to stabilize a non gravity gradient spacecraft within approximately 750 seconds. Numerous variations on this approach were then proposed and utilized including the energy based controller designed for NCUBE [18]. Most of the control methods used were developed for spacecraft with low eccentricity, medium to high inclination orbits and final states equal to a

nadir pointing attitude [19]. This is mainly due to the approach used, which was based on the periodic nature of the Earth's magnetic field in circular orbits of medium to high inclination.

In [20] Liang, et al, used RIOTS, a numerical solver, to accomplish a slewing maneuver in far less time using only magnetic torque. After converting the free final time optimal control problem into a fixed final time problem by adding state variables, they chose a minimum time cost function with end point penalties. Weighting parameters were determined through experimentation, and a model predictive controller was created to track the open loop solution. Simulating a non gravity gradient stabilized spacecraft in a circular, medium inclination orbit, this approach showed that slewing maneuvers could be completed approximately 50 times faster than had been possible with controllers based on the periodic nature of the magnetic field.

Following their lead, Yan, Fleming, Ross and Alfriend, used the spectral method to find the time optimal solutions for a rest to rest maneuver for NPSAT1, using only magnetic actuators. Yan found that solutions could be generated fast enough for real time application [21]. In [22] Yan, Ross and Alfriend proposed using the Legendre Pseudospectral Method outlined by Fahroo and Ross [23] for attitude stabilization using magnetic control in elliptic orbits. This approach, utilizing receding horizon control, reduced the computational time required by an order of magnitude when compared with methods based on the Riccati equation. In [24], Fahroo and Ross then used the pseudospectral method to solve infinite horizon optimal control problems of the type being used for 3-axis stabilization by Wisniewski and others. They used a quadratic cost function similar to the one used by Yan [21], with a modification to replace the time penalty with a cost for control torque, thus converting it into a fuel optimal problem. By minimizing the cost function subject to total torque constraints, they produced an optimal solution for the control torques required to stabilize the NPSAT 1 spacecraft from 30 deg to 0 deg in every axis in under

90 seconds. Their analysis was limited to a single source of torque, such as thrusters or momentum wheels, and did not address a combination system utilizing both magnetic torque and less constrained methods, such as reaction wheels or thrusters. Despite this, they proved that the pseudospectral method could not only provide an optimal fuel solution, but one that achieved the desired final state many times faster than the periodic methods based on the Riccati equation. Bedrossian and Bhatt applied the pseudospectral method to develop a zero propellant maneuver (ZPM) for the International Space Station. This application demonstrated the practicality and potential cost savings (over \$1 million in under three hours) of the pseudospectral method, although in this case, the command was generated offline and had to be uploaded to the spacecraft [25-27]. Zhou derived control algorithms combining magnetic torque systems with other sources to achieve consistent accuracy despite system degrades [28]. By using a collocation approach to solve for the magnetic torque control, rather than finding the solution via the Riccati method, researchers have demonstrated the capability for slewing maneuvers to a non-nadir pointing attitude in minutes rather than hours. Our method improves upon these collocation schemes to provide a system with all of the benefits of a traditional magnetic torque system - cheap to acquire, lightweight, and minimal fuel use - while reducing the limitations of past magnetic systems - nadir pointing only, slow response, confinement to low eccentricity/high inclination orbits.

Overall, the control designs for linearized attitude models are easily implemented, although the solution might not be optimal. In contrast, optimal solutions utilizing nonlinear dynamics are available, but the computational cost is too high for use in real time. This thesis presents a method utilizing the virtual motion camouflage (VMC) method to find near optimal solutions for attitude rotation. It accommodates user-defined constraints, provides near optimal

solutions with nonlinear dynamics and generates solutions rapidly in comparison to a baseline method.

This research addresses the problem of fuel optimal three-axis control for a CubeSat with magnetic torque coils mixed with thrusters. Specifically, rotations of a CubeSat with fixed initial and final times, states, and state derivatives are addressed. In Chapter 6, problem 1 is addressed - minimizing total torque, while in Chapter 7 problem 2, minimizing torque from the thrusters, is addressed. In both cases, a nearly optimal solution is sought with a significant reduction in computational cost.

The author's contributions to this thesis include the application of VMC with polynomial prey motion to problems 1 and 2 listed above, as well as evaluation of that application in 48 representative cases with various boundary conditions. After evaluation, VMC with polynomial prey motion was deemed effective when used with problem 1, but not effective with problem 2.

For this reason, VMC was then formulated using the B-Spline prey motion and applied to problem 2. Twenty four representative cases were evaluated using the VMC method augmented with the B-Spline prey motion. This method and B-Splines were both found to deliver near optimal results with a significant reduction in computational cost. Through experimentation, it was discovered that VMC is able to handle more severe path constraints than B-Splines and future work is suggested in this area to realize its full potential.

The thesis is organized as follows. In this chapter, background material is presented, including methods that were utilized in the past. In Chapter 2, the dynamics model is presented, along with the coordinate frames, and generation of a magnetic field model. The general VMC approach is described in Chapter 3 and the first of two representative problems is defined in

Chapter 4. This problem - minimizing the total torque - is solved using the VMC method with polynomial prey motion. The method is evaluated using several representative cases and found to provide near optimal solutions with significant reductions in computational cost as compared to the baseline solution. In Chapter 4, a similar comparison is made with the problem of the optimal attitude control management, using the B-Spline and the VMC augmented with the B-Spline prey motion to minimize the thruster torque in a system with both magnetic coils and thrusters. Performance is compared to the baseline approach and results are presented. Finally, a summary and suggestion of future work is presented in Chapter 6.



## CHAPTER 2: DYNAMICS MODEL

The quaternion based model is used to represent the attitude motion of the CubeSat. The kinematic relationship between the quaternion rates and the angular velocity is given by

$$\dot{\mathbf{q}} = \frac{1}{2} \begin{bmatrix} -\tilde{\omega}_B & \boldsymbol{\omega}_B \\ -\boldsymbol{\omega}_B^T & 0 \end{bmatrix} \mathbf{q} \quad (1)$$

in which  $\mathbf{q}$  is the quaternion,  $\boldsymbol{\omega}_B$  is the angular velocity and  $\tilde{\omega}_B$  is its skew symmetric matrix.

The CubeSat is assumed to be a rigid body in this thesis, and its attitude dynamics are modeled by

$$\begin{aligned} \dot{\omega}_B \mathbf{I}_m + \tilde{\omega}_B \mathbf{I}_m \boldsymbol{\omega}_B &= \mathbf{T} \\ \mathbf{T} &= \mathbf{T}_t + \mathbf{T}_c \end{aligned} \quad (2)$$

in which  $\mathbf{I}_m$  is the moment of inertia of the spacecraft,  $\mathbf{T}$  is the total torque,  $\mathbf{T}_t$  is the thruster torque, and  $\mathbf{T}_c$  is the magnetic coil torque, given by  $\mathbf{T}_c = \mathbf{m} \times \mathbf{B}_{bo}$ . The spacecraft is modeled with three pairs of thrusters, one pair per body axis, and three magnetic torque coils with reversible currents. The thruster torque  $\mathbf{T}_t$  in each axis is constrained by the total force available from a single thruster. A cold gas MEMS thruster [29] is assumed in this model, with its maximum force limited as  $|u_i| \leq 0.055 \text{ N}, i = 1, 2, 3$ . Assuming a moment arm for each thruster of 0.05m, the maximum thruster torque in each axis is then constrained according to

$$|T_{t,i}| - 0.00275 \text{ Nm} \leq 0 \quad i = 1, 2, 3 \quad (3)$$

The magnetic torque coils in this thesis are based primarily the parameters for the current UCF CubeSat design. Three magnetic torque coils are mounted on the  $+x$ ,  $+y$ , and  $+z$  sides of the spacecraft. Each coil has an area,  $a_c = 0.004879 \text{ m}^2$  and 80 turns of wire. The current is constrained according to

$$|i_i| - 0.210 \text{ A} \leq 0 \quad i = 1, 2, 3 \quad (4)$$

which leads to a corresponding constraint on the components of the moment  $\mathbf{M}$

$$|M_i| - 0.0820 \text{ Am}^2 \leq 0 \quad i = 1, 2, 3 \quad (5)$$

To ensure realistic angular rates, the maximum body rate is also constrained according to

$$|\omega_k| - 2\pi \leq 0 \quad (6)$$

Finally, the quaternion and body rates are constrained at the initial and final times, so

$$\mathbf{q}(t_0) - \mathbf{q}_0 = 0, \quad \mathbf{q}(t_f) - \mathbf{q}_f = 0, \quad \boldsymbol{\omega}(t_0) - \boldsymbol{\omega}_0 = 0, \quad \boldsymbol{\omega}(t_f) - \boldsymbol{\omega}_f = 0 \quad (7)$$

and since the quaternion is used, it is subject to the constraint

$$\mathbf{q}^T \mathbf{q} = 1 \quad (8)$$

### Coordinate Frames

Several coordinate frames are required to model the attitude dynamics produced by the spacecraft's interaction with the Earth's magnetic field. These systems include the Geocentric Equatorial System (IJK) [30], North East Down (NED), Local Vertical Local Horizon (LVLH) [31], Spacecraft Body (denoted by the subscript "bo"). In the IJK system,  $\hat{I}$  points at the vernal equinox,  $\hat{K}$  is aligned with the Earth's axis of rotation, and  $\hat{J}$  completes the right hand system.

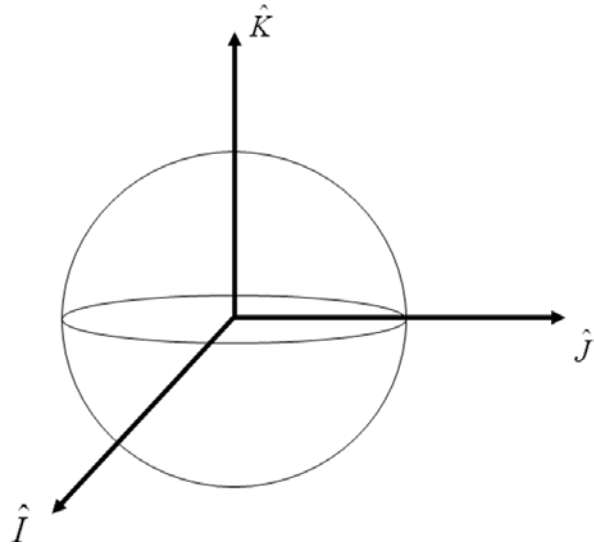


Figure 1. Geocentric Equatorial Coordinate Frame.

In the NED system,  $B_x$  points North,  $B_y$  points East, and  $B_z$  points in the negative vertical direction [32].

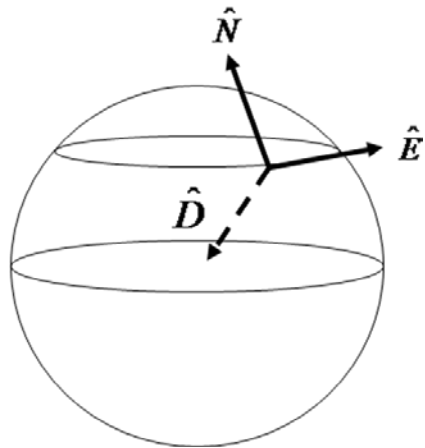


Figure 2. North, East, Down Coordinate Frame.

In the LVLH system,  $L_3$  points to the Earth's center,  $L_2$  points in the opposite direction of the angular momentum and  $L_1$ , which is approximately aligned with the velocity vector, completes the right hand coordinate system, i.e.  $L_1 = L_2 \times L_3$  [31].

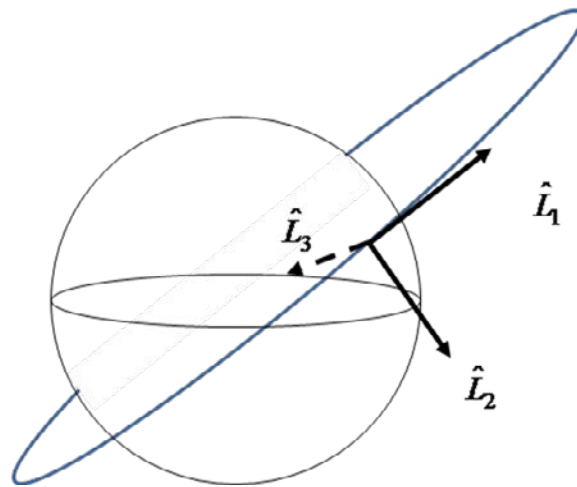


Figure 3. LVLH Coordinate Frame.

In the spacecraft body frame,  $\phi$  defines roll, a rotation about the  $x$  axis,  $\theta$  defines pitch, a rotation about the  $y$  axis, and  $\psi$  defines yaw, a rotation about the  $z$  axis. When the Euler angles are each set to  $0^\circ$ ,  $\hat{x}$  will be aligned with  $\hat{L}_1$ ,  $\hat{y}$  will be aligned with  $\hat{L}_2$  and  $\hat{z}$  will be aligned with  $\hat{L}_3$ .

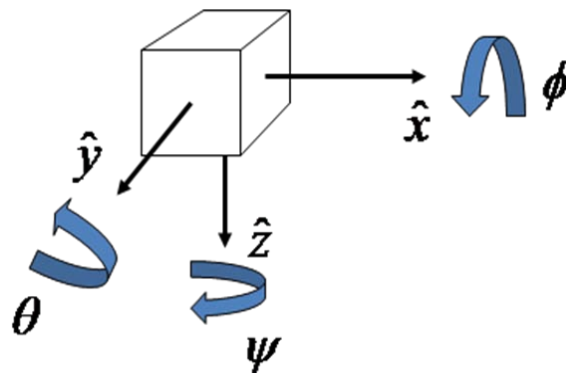


Figure 4. Rotations about the Spacecraft Body Coordinate Frame.

A 1-2-3 rotation sequence is used to convert Euler angles to quaternion form in this thesis.

## Magnetic Field Model

The orbital dynamics used in this method are based on two-body motion. The initial orbital elements are converted to  $\vec{r}_{IJK}$  and  $\vec{V}_{IJK}$  using the RANDV algorithm found in Vallado [30], and then used in conjunction with the Newton method to find an iterative solution to the universal Kepler's equation at each LGL node as outlined in [33]. The magnetic field model used is an 11<sup>th</sup> order and degree spherical harmonic model as outlined in [32], and modeled as the gradient of  $V$  where

$$V(r, \theta, \phi) = a \sum_{n=1}^k \left( \frac{a}{r} \right)^{n+1} \sum_{m=0}^n (g_n^m \cos m\phi + h_n^m \sin m\phi) P_n^m(\theta)$$

$$\mathbf{B} = -\Delta V \quad (9)$$

$a = 6371.2$  km,  $g_n^m$  and  $h_n^m$  are the IGRF Gaussian coefficients in the International Geomagnetic Reference Field Model (IGRF11) [34],  $r$  is the distance from the center of the Earth,  $\theta$  is the co-elevation, and  $\phi$  is the longitude. As in [32], the magnetic field components are first determined in the NED frame, then converted to the IJK reference frame using

$$B_I = (B_r \cos \delta + B_\theta \sin \delta) \cos \alpha - B_\phi \sin \alpha$$

$$B_J = (B_r \cos \delta + B_\theta \sin \delta) \sin \alpha + B_\phi \cos \alpha$$

$$B_K = (B_r \sin \delta - B_\theta \cos \delta) \quad (10)$$

where  $\alpha$  represents right ascension, and declination is defined by  $\delta \equiv 90^\circ - \theta$ . The longitude can be found using the right ascension and Greenwich sidereal time,  $\alpha_G$ , according to  $\phi = \alpha - \alpha_G$  [32]. The magnetic field is converted to LVLH using  $B_{LVLH} = QB_{IJK}$  where

$Q = [\hat{L}_1^T \quad \hat{L}_2^T \quad \hat{L}_3^T]^T$  is the rotation matrix, composed of the unit vectors of the LVLH system.

The magnetic field in body coordinates  $\mathbf{B}_{bo}$ , is then found using the transformation matrix [32].

$$A(q_k) = \begin{bmatrix} q_{1,k}^2 - q_{2,k}^2 - q_{3,k}^2 + q_{4,k}^2 & 2(q_{1,k}q_{2,k} + q_{3,k}q_{4,k}) & 2(q_{1,k}q_{3,k} - q_{2,k}q_{4,k}) \\ 2(q_{1,k}q_{2,k} - q_{3,k}q_{4,k}) & -q_{1,k}^2 + q_{2,k}^2 - q_{3,k}^2 + q_{4,k}^2 & 2(q_{2,k}q_{3,k} + q_{1,k}q_{4,k}) \\ 2(q_{1,k}q_{3,k} + q_{2,k}q_{4,k}) & 2(q_{2,k}q_{3,k} - q_{1,k}q_{4,k}) & -q_{1,k}^2 - q_{2,k}^2 + q_{3,k}^2 + q_{4,k}^2 \end{bmatrix}$$

$$\hat{\mathbf{B}}_{bo} = A(q_k)\hat{\mathbf{B}}_{LVLH} \quad (11)$$

Finally, the generated magnetic torque is calculated as  $\mathbf{M} = \mathbf{m} \times \mathbf{B}_{bo}$ . Figure 5, below, shows the moment,  $\mathbf{m}$ , which is created by the current (in red) flowing within a torque coil. It is easy to see that the forces generated (F1 and F3), will generate a torque,  $\mathbf{T}$ , to align  $\mathbf{m}$  with  $\mathbf{B}$ . At the same time, it is easy to see that a coil mounted on the top of the CubeSat in the picture would generate a moment  $\mathbf{m}$  that was parallel to  $\mathbf{B}$ . In this case,  $\mathbf{m} \times \mathbf{B}$  would yield no torque. This illustrates the reason why a set of 3 magnetic torque coils cannot generate torque in all three axes simultaneously, since any coil whose moment is parallel to the field is unable to generate torque.

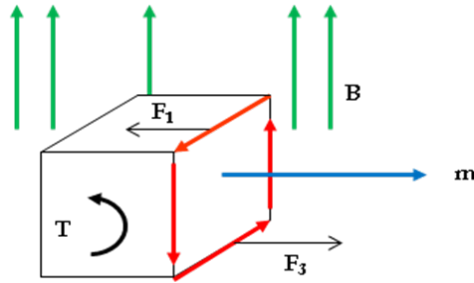


Figure 5. Magnetic coil interaction with magnetic field.  
Current is in red and flows around the coil in the magnetic field.

## Dimensionless Models

To aid the NLP solver in convergence, dimensionless quantities are used in all evaluated methods. In this case,  $\bar{m}=1$  kg and  $\bar{r}=0.05$  m are the dimensionless mass and length, respectively. The dimensionless velocity,  $\bar{V} = \bar{r} / (t_f - t_0)$  was assigned a value, 0.000125 m/s, with  $\bar{t} = \bar{r} / \bar{V}$  and the dimensionless current is chosen as  $\bar{i} = i_{\max} = 0.210$  A. Using these basic values, one can calculate dimensionless values for time, initial and final, time span (nodes for the NLP solver), acceleration, force, moment of inertia and Teslas.

$$\begin{aligned} \bar{t} &= \bar{r} / \bar{V}, \hat{t}_0 = t_0 / \bar{t}, \hat{t}_f = t_f / \bar{t}, \hat{t}_k = t_k / \bar{t} \quad \bar{g} = \bar{r} / \bar{t}^2 \\ \bar{F} &= \bar{m} / \bar{g}, \bar{J} = \bar{m} \bar{r}^2, \bar{B} = \bar{F} / (\bar{i} \bar{r}) \end{aligned} \quad (12)$$

These can then be applied to values for the actual moment of inertia, moment arm, maximum thruster force, maximum thruster torque, coil area, and magnetic field model (LVLH), yielding.

$$\begin{aligned} \hat{J}_{mom} &= J_{mom} / \bar{J}_{mom}, \hat{l} = l / \bar{r}, \hat{F}_{\max} = F_{\max} / \bar{F}, \hat{T}_{\max} = T_{\max} / (\bar{F} \bar{r}), \\ \hat{I}_{\max} &= I_{\max} / \bar{i}, \hat{a} = a / \bar{r}^2, \hat{B}_{LVLH} = B_{LVLH} / \bar{B} \end{aligned} \quad (13)$$

The next chapter will talk about the basic VMC approach, and how it is applied to two optimal attitude control problems, including the selection of prey motion.

### CHAPTER 3: VIRTUAL MOTION CAMOUFLAGE

In this chapter, the basic procedure of formulating the optimal trajectory design problem to a nonlinear programming problem via the VMC method is described. The detailed information about the VMC method can be found in [35], and in this chapter the application of this method to specific problems is described. The VMC approach begins by defining the attitude of the spacecraft  $\mathbf{x}_a(t) \in \mathfrak{R}^{n_a}$  as the aggressor motion in an  $n_a$ -dimensional space so that  $\mathbf{x}_a = \mathbf{q}$ . The aggressor motion, is a function of three items: a one-dimensional time varying path control parameter (PCP)  $v(t)$ , a virtual prey motion  $\mathbf{x}_p(t)$ , which can be defined as a polynomial, a B-Spline, or some other curve, and a time invariant reference point  $\mathbf{x}_r$ . Some coefficients of the prey motion are determined by the boundary conditions. The relation [35-36] among them is described by

$$\mathbf{x}_a(t) = \mathbf{x}_r + v(t)[\mathbf{x}_p(t) - \mathbf{x}_r] \quad (14)$$

For use in a nonlinear solver,  $v(t)$  will be discretized. Hesthaven [37] describes the Legendre expansion of a function  $v(t) \in L^2[-1,1]$  which can be approximated by

$$v(t) \approx I_N v(t) = \sum_{k=0}^N v(t_k) \phi_k(t) \quad (15)$$

where  $I_N$  is the interpolant of the function  $v(t)$ ,  $t_k$  represents the nodes at which the approximation is made, and  $\phi_k(t)$  represents the Lagrange interpolation polynomial [37]. The same form applies to the Legendre Gauss Lobatto (LGL) [23-24] or Legendre Gauss (LG) approximations [38], although the nodes and differentiation matrix will vary. As stated in



Hesthaven [37, if  $\phi_k(t)$  is differentiated and evaluated at the nodes, the derivative of  $v(t)$  can be found using

$$\dot{v}(t) \approx I_N \frac{d}{dt} I_N v(t_i) = \sum_{j=0}^N D_{ij} v(t_j) \quad (16)$$

where  $D$  is the  $(N+1) \times (N+1)$  differentiation matrix, found in [37]. For compact notation,  $D'_{ij}$  is defined by

$$D'_{ij} = 2 / (\hat{t}_f - \hat{t}_0) D_{ij} \quad (17)$$

The performance index  $J$  is discretized for use with the pseudospectral method as

$$J = \frac{t_f - t_0}{2} \left( \sum_{k=0}^N w_k \mathbf{u}_k^T \mathbf{u}_k \right) \quad (18)$$

for problems 1 and 2, where  $w_k$  denotes the weights for the  $k^{\text{th}}$  discretization node [37].

After representing all state and control variables as functions of the prey, reference, PCPs, and their derivatives, the optimal control problem becomes a parameter optimization problem which can be solved by any nonlinear programming solver. The parameters to be optimized are the PCP nodes  $v_k, k = 0 \dots N$  plus  $\mathbf{x}_r$ . Further development by Xu [35] has shown that the number of PCPs to be optimized can be reduced by calculating  $v_0, v_1, v_{N-1}$  and  $v_N$  when the initial and final state and state rate are known. The proof can be found in the Xu [35] and application of this will be seen in the first problem of minimizing total torque. This can reduce the number of PCP variables that need to be optimized from  $N+1$  to  $N-3$ . Compared with the baseline approach, this overall reduction in optimization parameters allows the optimal trajectory design problem to be solved much faster than baseline methods with a modest loss of optimality.

## CHAPTER 4: MINIMIZING THE TOTAL TORQUE

### Problem Definition

In this chapter, the problem is to find the optimal control that minimizes the performance index

$$J = \int_{t_0}^{t_f} \mathbf{T}^T \mathbf{T} dt \quad (19)$$

which represents the total torque used for attitude control on a CubeSat with a single source of torque (thrusters in this case). In this problem, the spacecraft is assumed to have only one source of torque - thrusters. The attitude dynamics are described by Eqs. 1-2, subject to the inequality constraints on thruster torque and maximum body rate as noted in Eqs. 3 and 6. The system is also subject to equality constraints related to the boundary conditions and the quaternion, noted in Eqs. 7 and 8, respectively.

This problem will be solved using VMC with the polynomial prey motion and compared to the baseline approach. The aggressor motion  $\mathbf{x}_a = \mathbf{q}_a = [q_{a,1} \quad q_{a,2} \quad q_{a,3} \quad q_{a,4}]^T$  is the quaternion describing the attitude of the chaser spacecraft in the body fixed coordinate frame.

### Necessary Conditions

Since the initial and final states are fixed, the optimal solution  $\mathbf{q}_a$  must satisfy the following equations:

$$\mathbf{q}_{a,0} = \mathbf{q}_0 \quad \mathbf{q}_{a,N} = \mathbf{q}_f \quad (20)$$

For VMC, we also need to satisfy

$$\mathbf{q}_{a,0} = \mathbf{q}_r + v_0 (\mathbf{q}_{p,0} - \mathbf{q}_r) \quad \mathbf{q}_{a,N} = \mathbf{q}_r + v_N (\mathbf{q}_{p,N} - \mathbf{q}_r) \quad (21)$$

If we let  $v_0 = v_N = 1$ ,  $\mathbf{q}_{p,0} = \mathbf{q}_0$ , and  $\mathbf{q}_{p,N} = \mathbf{q}_f$  then it can be seen that the optimized solution  $\mathbf{q}_a$  will always satisfy the boundary conditions for the state.

$$\mathbf{q}_{a,0} = \mathbf{q}_{p,0} = \mathbf{q}_0 \quad \mathbf{q}_{a,N} = \mathbf{q}_{p,N} = \mathbf{q}_f \quad (22)$$

Since the initial and final state rates are fixed, the derivative of the optimized state solution must satisfy  $\dot{\mathbf{q}}_{a,0} = \dot{\mathbf{q}}_0$   $\dot{\mathbf{q}}_{a,N} = \dot{\mathbf{q}}_f$  to meet the boundary conditions. Based on Eq. 16, the following relations must also be known to be true

$$\dot{\mathbf{q}}_{a,0} = \sum_{k=0}^N D'_{0,k} \mathbf{q}_a \quad \dot{\mathbf{q}}_{a,N} = \sum_{k=0}^N D'_{N,k} \mathbf{q}_a \quad (23)$$

Utilizing these known relations and with some manipulation (details in Xu [35]),  $v_1$  and  $v_{N-1}$  can be found via

$$\begin{bmatrix} v_1 \\ v_{N-1} \end{bmatrix} = \begin{bmatrix} a_{11} & a_{12} \\ a_{21} & a_{22} \end{bmatrix}^{-1} \begin{bmatrix} \dot{\mathbf{q}}_{a,i,0} - v_0 \dot{\mathbf{q}}_{p,i,0} - D'_{00} v_0 a_1 - \sum_{k=2}^{N-2} D'_{0k} v_k a_1 - D'_{0N} v_N a_1 \\ \dot{\mathbf{q}}_{a,i,N} - v_N \dot{\mathbf{q}}_{p,i,N} - D'_{N0} v_0 b_1 - \sum_{k=2}^{N-2} D'_{Nk} v_k b_1 - D'_{NN} v_N b_1 \end{bmatrix} \quad (24)$$

where

$$\begin{aligned} a_{11} &= D'_{01} a_1 & a_{12} &= D'_{0,N-1} a_1 & a_{21} &= D'_{N,1} b_1 & a_{22} &= D'_{N,N-1} b_1 \\ a_1 &= q_{p,i,0} - q_{r,i} & b_1 &= q_{p,i,N} - q_{r,i} & i &= 2 \end{aligned} \quad (25)$$

Equations 23-24 calculate a  $v_1$  and a  $v_{N-1}$  that will ensure the optimized state solution,  $\mathbf{q}_a$ , will satisfy the boundary conditions for the state derivative at  $t_i$  and  $t_{N-1}$  when used to calculate  $\mathbf{q}_a$  in Eq. 14.

### Generating Prey Motion and Path Control Parameters

If the prey motion is calculated prior to the optimization loop and remains fixed during optimization, the computation cost will be lower than if the parameters describing the prey motion must be optimized along with the PCPs. Conversely, a fixed prey motion is less flexible. For this reason, problems that require less flexibility in the curves (such as the problem of minimizing total torque) can achieve near optimal solutions with a fixed prey motion, while other problems, such as the one described in Chapter xx, may require a prey motion that is also optimized.

With four fixed states and state rate boundary conditions, all four coefficients,  $a_i, b_i, c_i, d_i$ , required to describe a 3rd order polynomial curve (used for the prey motion) can be determined prior to the optimization loop. The prey motion and its derivative for the  $i$ th dimension are calculated using the polynomial

$$q_{p,i,k} = \frac{1}{3}a_i t_k^3 + \frac{1}{2}b_i t_k^2 + c_i t_k + d_i \quad i=2 \quad k=0 \dots N \quad (26)$$

and its derivative

$$\dot{q}_{p,i,k} = a_{q,i} t^2 + b_{q,i} t + c_{q,i} \quad i=2 \quad k=1 \dots N-1 \quad (27)$$

The values for  $v_0, v_1, v_{N-1}$  and  $v_N$  are calculated as mentioned in the previous section. The parameters to be optimized in the nonlinear solver are  $\mathbf{q}_r$  and  $v_k$  for  $k=2 \dots N-2$ . The PCPs are constrained according to  $-2 \leq v_k \leq 2$ . An initial guess of  $v_k = 1$  is chosen for  $k=2 \dots N-2$ .

The initial guess is  $\mathbf{q}_r = [0 \quad 0 \quad 0 \quad 1]^T$ .

The prey motion  $\mathbf{q}_{p,k}$  is initialized by calculating a value for  $q_{p,i,k}$ , and  $\dot{q}_{p,i,k}$  at each node and at 1 of the 4 dimensions, using Eqs. (25-26). In this case,  $i = 2$ . The prey motion for the  $j$ th dimensions ( $j=1,3,4$ ),  $N=1,N-1$  is calculated as

$$\begin{bmatrix} \mathbf{q}_{p,j,1} \\ \mathbf{q}_{p,j,N-1} \end{bmatrix} = \begin{bmatrix} D_{01} & D_{0,N-1} \\ D_{N1} & D_{N,N-1} \end{bmatrix}^{-1} \begin{bmatrix} \dot{\mathbf{q}}_{p,j,0} - D_{00} \mathbf{q}_{p,j,0} - \sum_{k=2}^{N-2} D_{0k} \mathbf{q}_{p,j,k} - D_{0N} \mathbf{q}_{p,j,N} \\ \dot{\mathbf{q}}_{p,j,N} - D_{N0} \mathbf{q}_{p,j,0} - \sum_{k=2}^{N-2} D_{Nk} \mathbf{q}_{p,j,k} - D_{NN} \mathbf{q}_{p,j,N} \end{bmatrix} \quad (28)$$

Then the prey motion for the  $j$ th dimensions ( $j=1,3,4$ ) and  $k=0,3\dots N-2,N$  is calculated by substituting  $j$  for  $i$  in Eq. 28. The next section will show how this prey motion is applied.

#### Application - Minimize Total Torque

The PCPs were calculated in the previous section and are used with Eq. 16 to find  $\dot{v}$

$$\dot{v}_k = \sum_{l=0}^N D_{k,l} v_l \quad (29)$$

The aggressor motion is calculated according to

$$\mathbf{q}_{a,k} = \mathbf{q}_r + v_k (\mathbf{q}_{p,k} - \mathbf{q}_r) \quad k = 0 \dots N \quad (30)$$

which is normalized since it is a quaternion according to

$$\mathbf{q}_{a,k} = \frac{\mathbf{q}_{a,k}}{\|\mathbf{q}_{a,k}\|} \quad k = 0 \dots N \quad (31)$$

Since  $\dot{\mathbf{q}}_r = \ddot{\mathbf{q}}_r = \mathbf{0}$  the derivative of the aggressor motion for  $k = 1 \dots N - 1$  is calculated according to

$$\dot{\mathbf{q}}_{a,k} = \dot{v}_k (\mathbf{q}_{p,k} - \mathbf{q}_r) + v_k (\dot{\mathbf{q}}_{p,k}) \quad (32)$$

The aggressor motion  $\mathbf{q}_{a,k}$  is then used to calculate the corresponding body rates  $\boldsymbol{\omega}_k$ .

$$\boldsymbol{\omega}_k = \left( \tilde{\mathbf{q}}_{a,1-3,k} + q_{a,4,k} \mathbf{I} \right)^{-1} 2\dot{\mathbf{q}}_{a,k} \quad k = 0 \dots N \quad (33)$$

The derivative of the body rates can be found using Eq. 16.

$$\dot{\boldsymbol{\omega}}_k = \sum_{l=0}^N D'_{k,l} \boldsymbol{\omega}_l \quad (34)$$

Then the total torque  $\mathbf{T}$  at each node is found using

$$\mathbf{T}_k = \dot{\boldsymbol{\omega}}_k \mathbf{I}_{mom} + \tilde{\boldsymbol{\omega}}_k \mathbf{I}_{mom} \boldsymbol{\omega}_k \quad (35)$$

where the moment of inertia tensor is given by

$$\mathbf{I}_{mom} = 0.0009 \mathbf{I}_{3 \times 3} \quad \text{kg m}^2 \quad (36)$$

### Simulation Scenario And Discussion

The scenario presented simulates a CubeSat with a moment of inertia  $\mathbf{I}_m = \text{diag}(0.0009, 0.0009, 0.0009)$ . The CubeSat is fitted with only one source of torque - thrusters - with three pairs of thrusters mounted on three different locations to provide control torque in each body axis. The VMC (with polynomial prey motion) solution presented here is evaluated against a baseline approach. The baseline solution is found by converting the original optimal control problem to an NLP via the LGL pseudospectral collocation method. State rates and control forces are calculated through differential inclusion in both the VMC and baseline approaches. The simulation is run on a CPU with an Intel Q9000 processor running at 2.00 GHz, running MATLAB Version 7.8.0 (R2009a).

A total of forty eight cases were evaluated. The points were chosen so that the initial Euler angle offset varied from -40 to 40 degrees and the initial body rates varied from -4 to 4 deg/s. A final time of  $t_f = 70 s$  was used for this problem. Each set of initial conditions was evaluated for performance error (as a percentage of the difference between the baseline and VMC solution), and percentage of CPU computational time reduction. In general, the VMC algorithm delivered solutions that were very similar (and sometimes better) than that of the baseline approach, but much quicker. Figure 6 shows the percentage of performance index error (above) and percent reduction in computational time (below, in parentheses) for the VMC solution as compared to the baseline approach. From the values, it is easy to see that VMC reduces the computational cost - sometimes up to 99% - while delivering solutions that are near optimal (performance index errors that were typically under 1% for individual points, with a maximum error of less than 4%).

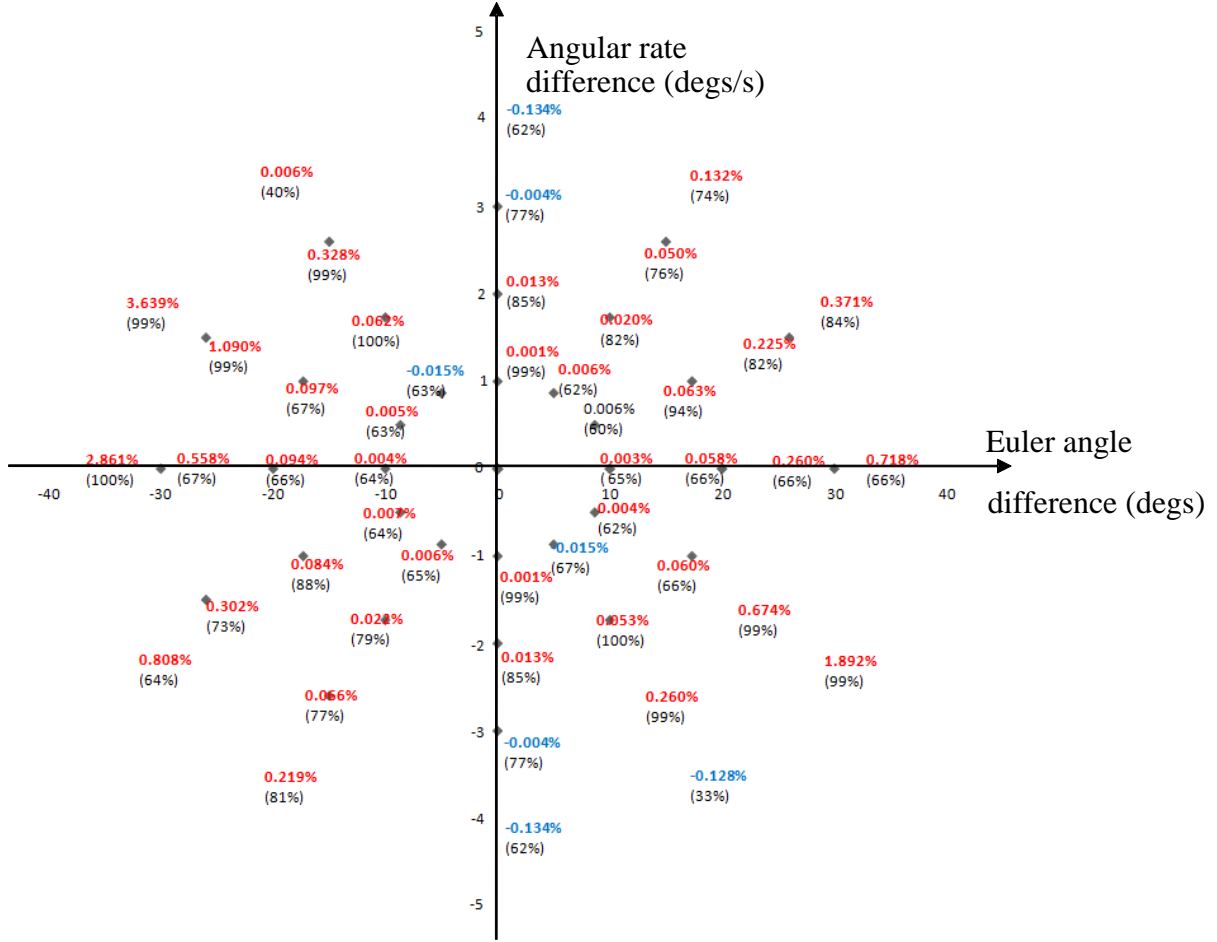


Figure 6. Performance error between the Baseline and VMC with polynomial prey motion.

Tables 1 is included to show the optimality and computational cost using VMC with polynomial prey motion in comparison to the baseline approach for one example case. For the specific example shown in Table 1, the initial and final quaternions were calculated as  $\mathbf{q}_0 = [0.1921 \ 0.4119 \ 0.1921 \ 0.8698]^T$  and  $\mathbf{q}_f = [0 \ 0 \ 0 \ 1]^T$ , respectively. This corresponds to an initial Euler angles of  $40^\circ$  and a final Euler angles of  $0^\circ$  in each axis, using a 1-2-3 rotation sequence to convert the Euler angles to quaternions. The initial quaternion rate is



assumed to be  $\dot{\mathbf{q}}_0 = [0.0095 \ 0.0076 \ 0.0057 \ -0.0069]^T$  and the final rate of 0 deg/sec converted to  $\dot{\mathbf{q}}_f = [0 \ 0 \ 0 \ 0]^T$ .

Table 1. Total torque problem, results comparison (Polynomial prey motion).

N	Baseline Solution J (N <sup>2</sup> m <sup>2</sup> s)	Baseline Solution CPU(s)	VMC Solution J (N <sup>2</sup> m <sup>2</sup> s)	VMC Solution CPU(s)
8	9.2695E-12	4.68	9.4226E-12	1.93
15	9.2709E-12	15.43	9.4225E-12	1.81
20	9.2718E-12	24.30	9.4179E-12	4.62
25	9.2709E-12	44.75	9.4279E-12	7.75

The VMC solution is found to be within 2% of the baseline solution with the same number of nodes. Additionally, the VMC solution for 8 nodes was within 2% of the 25 node baseline solution and it was 96% faster.

Figure 7 shows the VMC state solution in quaternion form for the 8-node case. The plot is smooth, meets the boundary conditions and obeys all constraints.

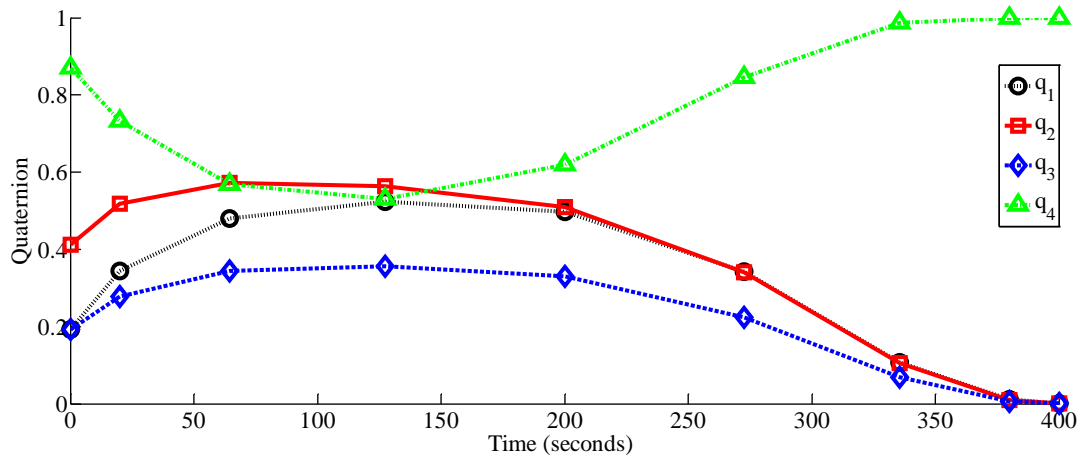


Figure 7. Quaternion of the near optimal attitude trajectory.

The same is true for the state rates or body rates. The plot shows smooth lines with a reasonable magnitude that satisfies all boundary conditions.

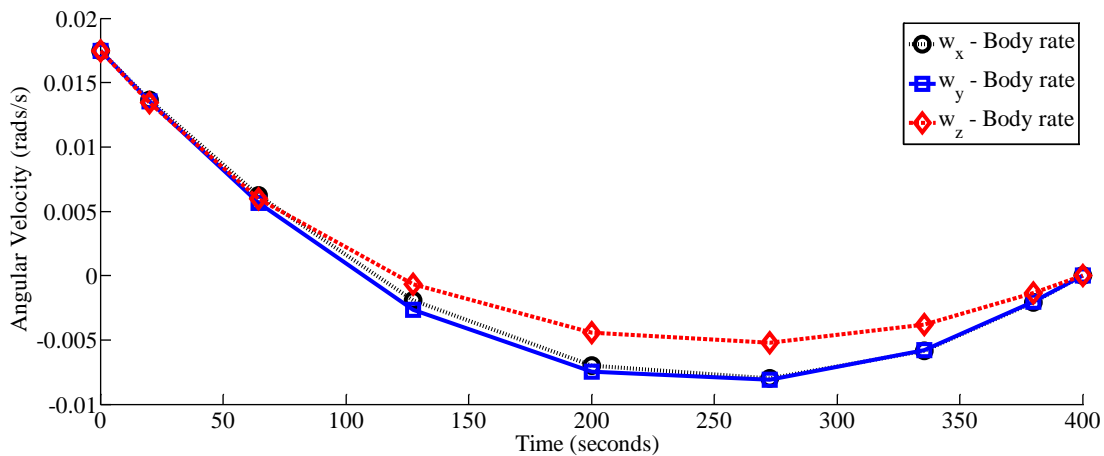


Figure 8. Angular velocity of the near optimal attitude trajectory.

Figure 9 shows a comparison of the commanded torque from the VMC and baseline solutions. Although there is some variation in this plot, it is small and both curves show a control that is smooth enough for actual hardware to follow. Again, the solution remains within the constraints listed in the problem definition.

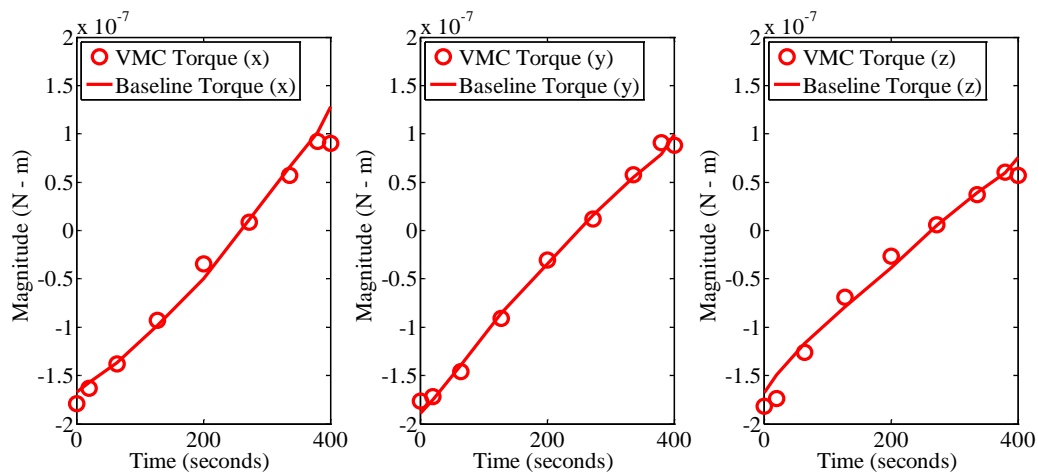


Figure 9. VMC control torque for near optimal rotation.

From the results in Figure 6 and Table 1, one can see that VMC with polynomial prey motion produces results that are very near the baseline solution. In Figures 7, 8 & 9, one can see that

these near optimal results produce the rotations using commands that are smooth enough to be easily implemented in actual hardware.

It is important to note that this thesis assumes continuous thrust with no lower bounds on the thrust. Any implementation in real hardware would surely include some lower bounds on the thrust produced by each thruster, and possibly include constraints for time between pulses. It is anticipated that a pulse width modulation scheme would be used to utilize the solutions found through VMC. This will be discussed in Chapter 6, Summary and Future Work.

## CHAPTER 5: ATTITUDE CONTROL MANAGEMENT

### Problem Definition

In this chapter, the problem is to find the optimal control that minimizes the performance index

$$J = \int_{t_0}^{t_f} \mathbf{T}_{tot}^T \mathbf{T}_{tot} dt + 10 \frac{\int_{t_0}^{t_f} \mathbf{T}_{thr}^T \mathbf{T}_{thr} dt}{\int_{t_0}^{t_f} \mathbf{T}_{tot}^T \mathbf{T}_{tot} dt} \quad (37)$$

which is designed to minimize the thruster torque in a system with both magnetic torque coils and thrusters, while still providing a solution that is smooth enough for implementation. The attitude dynamics are given by Eqs. 1-2. and the system is subject to inequality constraints on thruster torque, magnetic moment, and maximum body rate according to Eqs. 3, 5 and 6, respectively. The system is also subject to equality constraints for the boundary conditions and the quaternion, according to Eqs. 7 and 8.

This problem will be solved using VMC with the B-Spline prey motion and compared both the B-Spline and baseline approach. The final time for this problem is fixed at  $t_f = 400s$ .

### Generating Prey Motion and Path Control Parameters

The prey motion in this case will be generated using non-uniform open b-splines to create 4 curves - one for each element of the quaternion. Each B-Spline curve (and its derivative) is calculated by

$$\mathbf{C}(\hat{t}_k) = \sum_{i=0}^n N_{i,p}(\hat{t}_k) \mathbf{P}_i \quad \hat{t}_0 \leq \hat{t}_k \leq \hat{t}_f \quad (38)$$

$$\mathbf{C}'(\hat{t}_k) = \sum_{i=0}^n N'_{i,p}(\hat{t}_k) \mathbf{P}_i \quad \hat{t}_0 \leq \hat{t}_k \leq \hat{t}_f \quad (39)$$

where  $\mathbf{C}(\hat{t}_k)$  is the curve evaluated at each LGL node,  $\mathbf{P}_i$  represents the control points and  $N_{i,p}(\hat{t}_k)$  denotes the basis functions [39]. The number of elements in the knot vector can be found using the equation  $m = n + p + 1$ , where  $p$  is the degree of the curve and  $n + 1$  is the number of control points. In this thesis, the prey motion is defined by a B-Spline curve using an with  $n = p = 5$ , so the knot equation given by  $U = \{\underbrace{\hat{t}_0, \dots, \hat{t}_0}_{p+1}, \hat{t}_{p+1}, \dots, \hat{t}_{m-p-1}, \underbrace{\hat{t}_f, \dots, \hat{t}_f}_{p+1}\}$  collapses to  $U = \{\underbrace{\hat{t}_0, \dots, \hat{t}_0}_{p+1}, \underbrace{\hat{t}_f, \dots, \hat{t}_f}_{p+1}\}$ . Following the procedure in Piegl [39], the basis functions and their derivatives are calculated according to

$$N_{i,0}(\hat{t}_k) = \begin{cases} 1 & \text{if } U_i \leq \hat{t}_k \leq U_{i+1} \\ 0 & \text{otherwise} \end{cases} \quad i = 0 \dots n$$

$$N_{i,p}(\hat{t}_k) = \frac{\hat{t}_k - U_i}{U_{i+p} - U_i} N_{i,p-1}(\hat{t}_k) + \frac{U_{i+p+1} - \hat{t}_k}{U_{i+p+1} - U_{i+1}} N_{i+1,p-1}(\hat{t}_k)$$

$$N'_{i,p} = \frac{p}{U_{i+p} - U_i} N_{i,p-1}(\hat{t}_k) - \frac{p}{U_{i+p+1} - U_{i+1}} N_{i+1,p-1}(\hat{t}_k) \quad (40)$$

The first and last control points are determined by the boundary conditions for the quaternion:  $\mathbf{P}_0 = \mathbf{q}_0$ ,  $\mathbf{P}_n = \mathbf{q}_f$ . The middle control points,  $\mathbf{P}_{1 \dots n-1}$ , come from the initial guess. For use with the direct collocation method, the non dimensional time vector  $\hat{\mathbf{t}}$  represents the LGL nodes. Finally, the prey motion  $\mathbf{q}_p$  and its derivative  $\dot{\mathbf{q}}_p$ , are calculated using Eqs. 38 and 39. Note that

if  $n = p$ , the knot vector is composed solely of  $\mathbf{q}_0$  and  $\mathbf{q}_f$ , allowing the basis function and its derivative to be calculated outside the optimization loop to reduce computational time.

### Application

The parameters to be optimized in the nonlinear solver are  $\mathbf{P}_i$ ,  $\mathbf{q}_r$  and  $v_k$  for  $i = 2 \dots n$  and  $k = 1 \dots N - 1$ . In this application, the control point elements, reference point elements and path control parameters were constrained according to  $-3 \leq P_{i,j} \leq 3$ ,  $-1 \leq q_{r,j} \leq 1$  and  $0.8 \leq v_k \leq 1.2$ , respectively, for  $i = 1 \dots n - 1$ ,  $j = 1 \dots 4$  and  $k = 2 \dots N - 2$ . It is noted that some tuning is typically required to determine the appropriate bounds for a specific application.

The prey motion  $\mathbf{q}_{p,i,k}$  and its derivative  $\dot{\mathbf{q}}_{p,i,k}$  are generated as B-Spline curves according to the procedure in the previous section. As in Chapter 4, the states and state rates are fixed, so  $v_0 = v_N = 1$ . The remaining PCPs come from the optimization variables and the derivative of the PCPs can be found using

$$\dot{v}_k = \sum_{l=0}^N D'_{k,l} v_l \quad (41)$$

The aggressor motion (and its derivative) for  $k = 0, N$  come from the boundary conditions and the aggressor motion for  $k = 1 \dots N - 1$  is calculated according to

$$\mathbf{q}_{a,k} = \mathbf{q}_r + v_k (\mathbf{q}_{p,k} - \mathbf{q}_r) \quad (42)$$

The state rate  $\dot{\mathbf{q}}_a$  is determined using

$$\dot{\mathbf{q}}_{a,k} = \sum_{l=0}^N D'_{k,l} \mathbf{q}_{a,k} \quad k = 0 \dots N \quad (43)$$

The body rates can then be found from the quaternion and its derivative using the following equation found in Chobotov [40]:

$$\begin{aligned}
\omega_{1,k} &= 2(q_{4,k}\dot{q}_{1,k} + q_{3,k}\dot{q}_{2,k} - q_{2,k}\dot{q}_{3,k} - q_{1,k}\dot{q}_{4,k}) \\
\omega_{2,k} &= 2(-q_{3,k}\dot{q}_{1,k} + q_{4,k}\dot{q}_{2,k} + q_{1,k}\dot{q}_{3,k} - q_{2,k}\dot{q}_{4,k}) \\
\omega_{3,k} &= 2(q_{2,k}\dot{q}_{1,k} - q_{1,k}\dot{q}_{2,k} + q_{4,k}\dot{q}_{3,k} - q_{3,k}\dot{q}_{4,k}) \quad k = 0 \dots N
\end{aligned} \tag{44}$$

and the derivative of those body rates is found according to

$$\dot{\omega}_k = \sum_{l=0}^N D'_{k,l} \omega_l \tag{45}$$

Then the total torque desired  $\mathbf{T}$  at each node is found using

$$\mathbf{T}_k = \dot{\omega}_k \mathbf{I}_{mom} + \tilde{\omega}_k \mathbf{I}_{mom} \omega_k \tag{46}$$

At this point it is desirable to calculate a magnetic moment given the total torque required and the magnetic field in the spacecraft body frame. By calculating the moment, rather than optimizing the moment at each LGL node, the computational cost can be kept much lower. A procedure developed by Sidi [41] for use in a gravity gradient stabilized spacecraft is adapted for use here to calculate this magnetic moment. Since the coil torque is given by  $\hat{\mathbf{T}}_c = (\hat{\mathbf{M}} \times \hat{\mathbf{B}}_{bo})$

$$\begin{bmatrix} \hat{\mathbf{T}}_{cx} \\ \hat{\mathbf{T}}_{cy} \\ \hat{\mathbf{T}}_{cz} \end{bmatrix} = \begin{bmatrix} 0 & \hat{\mathbf{B}}_{bo,z} & -\hat{\mathbf{B}}_{bo,y} \\ -\hat{\mathbf{B}}_{bo,z} & 0 & \hat{\mathbf{B}}_{bo,x} \\ \hat{\mathbf{B}}_{bo,y} & -\hat{\mathbf{B}}_{bo,x} & 0 \end{bmatrix} \begin{bmatrix} \hat{\mathbf{M}}_x \\ \hat{\mathbf{M}}_y \\ \hat{\mathbf{M}}_z \end{bmatrix} \tag{47}$$

and it is desired to find  $\hat{\mathbf{M}}$  given  $\hat{\mathbf{T}}_c$  and  $\hat{\mathbf{B}}_{bo}$ , it is natural to try to invert the 3x3 matrix in the process of finding for the moment. Unfortunately, in this case the matrix is singular, and another

method must be used. At the same time, it is easy to see that ensuring the moment is perpendicular to the magnetic field will maximize the torque. After some manipulation, one can form an equation that utilizes this fact to find the desired moment.

$$\begin{aligned}\hat{\mathbf{B}}_{bo} \times \hat{\mathbf{T}}_c &= \hat{\mathbf{B}}_{bo} \times (\hat{\mathbf{M}} \times \hat{\mathbf{B}}_{bo}) \\ \hat{\mathbf{B}}_{bo} \times (\hat{\mathbf{M}} \times \hat{\mathbf{B}}_{bo}) &= (\hat{\mathbf{B}}_{bo} \cdot \hat{\mathbf{B}}_{bo}) \hat{\mathbf{M}} - (\hat{\mathbf{B}}_{bo} \cdot \hat{\mathbf{M}}) \hat{\mathbf{B}}_{bo}\end{aligned}\quad (48)$$

Since  $(\hat{\mathbf{B}}_{bo} \cdot \hat{\mathbf{M}}) = 0$  when  $\hat{\mathbf{M}}$  is perpendicular to the Earth's magnetic field, the second term can be set equal to zero, yielding  $\hat{\mathbf{B}}_{bo} \times \hat{\mathbf{T}}_c = (\hat{\mathbf{B}}_{bo} \cdot \hat{\mathbf{B}}_{bo}) \hat{\mathbf{M}}$  and finally

$$\hat{\mathbf{M}} = \frac{1}{\|\hat{\mathbf{B}}_{bo}\|^2} (\hat{\mathbf{B}}_{bo} \times \hat{\mathbf{T}}_c) \quad (49)$$

where  $\hat{\mathbf{B}}_{bo}$  is the dimensionless magnetic field in body coordinates and  $\hat{\mathbf{T}}$  is the total torque required. Then the torque from the coils is given by  $\hat{\mathbf{T}}_c = (\hat{\mathbf{M}} \times \hat{\mathbf{B}}_{bo})$  and the torque required from the thrusters is  $\hat{\mathbf{T}}_t = \hat{\mathbf{T}} - \hat{\mathbf{T}}_c$ .

### Simulation Results and Discussion

The scenario presented simulates a CubeSat with a moment of inertia  $\mathbf{I}_m = \text{diag}(0.0009, 0.0009, 0.0009)$ . The target orbit in this scenario is defined by the following orbital elements which are assumed to be constant throughout the simulation: semi-major axis  $a = 7709.04$  km, eccentricity  $e = 0.1$ , inclination  $i_n = 35.4^\circ$ , right ascension of the ascending node  $\Omega = 0^\circ$ , argument of perigee  $\omega_{aop} = 0^\circ$ , and initial true anomaly  $f = 0^\circ$ . Given that much of the recent literature on magnetic torque control has centered around the NPSAT-1 mission,



this simulation uses similar orbital elements to aid in comparison. The VMC with B-Spline prey motion solution is evaluated against the B-Spline and a baseline approach. The baseline solution is found by converting the original optimal control problem to an NLP via the LGL pseudospectral collocation method. State rates and control forces are calculated through differential inclusion in the B-Spline, VMC with B-Spline prey motion and baseline approaches. The simulation is run on a CPU with an Intel Q9000 processor running at 2.00 GHz, running MATLAB Version 7.8.0 (R2009a).

A total of twenty four cases were evaluated. The points were chosen so that the initial Euler angle offset varied from 0 to 90 degrees and the initial body rates varied from 0 to 1deg/s.

Table 2. Boundary Conditions used to evaluate solutions for problem 2.

Initial Euler Angles (deg)	Final Euler Angles (deg)	Initial Body Rates (deg/s)	Final Body Rates (deg/s)	Initial Euler Angles (deg)	Final Euler Angles (deg)	Initial Body Rates (deg/s)	Final Body Rates (deg/s)
15	0	1	0	-15	0	1	0
30	0	1	0	-30	0	1	0
45	0	1	0	-45	0	1	0
60	0	1	0	-60	0	1	0
75	0	1	0	-75	0	1	0
90	0	1	0	-90	0	1	0
0	15	0	0	0	-15	0	0
0	30	0	0	0	-30	0	0
0	45	0	0	0	-45	0	0
0	60	0	0	0	-60	0	0
0	75	0	0	0	-75	0	0
0	90	0	0	0	-90	0	0

Each set of initial conditions was evaluated for performance index error (as a percentage of the difference between the method evaluated and the baseline solution), and percentage of CPU computational time reduction (as compared to the baseline approach). Overall, the computational time was reduced by 86% as compared to the baseline using B-Splines and by 17% using VMC with B-Spline prey motion. At the same time, the performance index was within 1.5% of the baseline solution for the B-Spline approach and within 1.6% of the baseline solution for the VMC with B-Spline prey motion.

The differences in computational time are closely related to the number of parameters to be optimized. The B-Spline approach, with  $n=p=6$ , evaluated at times corresponding to 10 LGL nodes, requires 20 parameters to be optimized. The VMC with B-Spline prey motion, with  $n=p=5$  and 10 LGL nodes, requires 29 parameters to be optimized. The baseline approach, with 10 LGL nodes, requires 36 parameters to be optimized. The simulation results show that the B-Spline is the fastest, followed by the VMC with B-Spline prey motion and the baseline, which is significantly slower. This makes sense given that the B-Spline has the lowest number of optimization parameters, and is flexible enough (with 7 total control points) to create a curve that meets the constraints in this case.

When the path constraints are increased, the situation is expected to change. For any curve with path constraints that require variation from a straight line, the B-Spline will need additional control points to generate a curve that stay within those constraints. As these type of path constraints increase, more control points will be required. Figure 10 illustrates the first case where the path constraints do not interfere with a straight line between the end points.

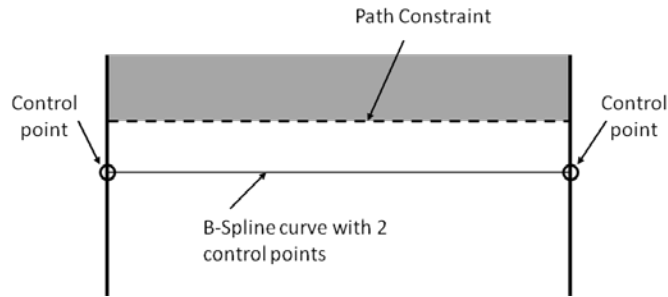


Figure 10. B-Spline curve with path constraints that do not interfere with a straight line between end points.

The next case, where a path constraint does interfere with a straight line between end points, is illustrated in Figure 11. In this case, a third control point is required to generate a curve that obeys the path constraint.

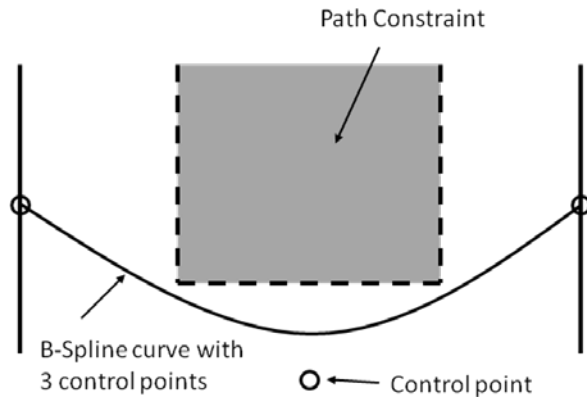


Figure 11. B-Spline curve with a path constraint that drives requirement for at least one additional control point.

Figure 12 illustrates the situation as additional path constraints are added which further interfere with any straight line path.

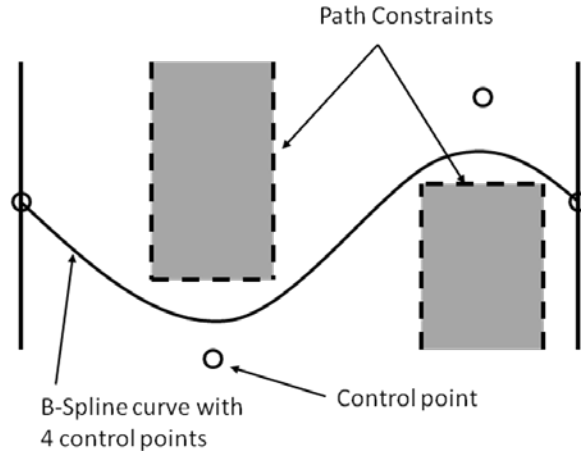


Figure 12. B-Spline curve with two path constraints which drive a requirement for at least four control points.

Each new constraint of this type drives the requirement for another control point. And each additional interior control point increases the number of parameters to be optimized by the number of dimensions (for example, the number of parameters to be optimized would increase by four per path constraint for the problems presented in this thesis). It is easy to see how additional path constraints of this type could cause the computational cost for the B-Spline method to increase. Conversely, the VMC with B-Spline prey motion can "get around" each additional path constraint by adding just one PCP per constraint for all four dimensions. As a result, VMC with B-Spline prey motion is expected to generate solutions faster than a B-Spline algorithm when significant path constraints are present, requiring additional control points. In Problem 2, no path constraints of this type were present. As a result, VMC with B-Spline prey motion was not substantially faster than B-Spline in the simulation for Problem 2.

Table 3 compares the B-Spline and VMC with B-Spline prey motion to the baseline approach in for a specific case. The example shown in Table 3 is based on the commanded rotation of a CubeSat from an initial attitude  $\mathbf{q}_0 = [0.0307 \quad 0.7037 \quad 0.0307 \quad 0.7091]$  and body

rate,  $\boldsymbol{\omega}_0 = [0.0175 \ 0.0175 \ 0.0175]$  to a final attitude of  $\boldsymbol{q}_0 = [0 \ 0 \ 0 \ 1]$  and body rate of  $\boldsymbol{\omega}_f = [0 \ 0 \ 0]$ . This is equivalent to an initial offset angle of 85 deg and body rate of 1 deg/s in every axis, and a final state of 0 deg and 0 deg/s, and is meant to simulate a CubeSat at an arbitrary attitude and body rate, which is desired to be returned to a nadir pointing attitude. The final time is fixed at 400 sec, and the total torque, magnetic moment, and maximum body rate are constrained as stated in the Problem definition.

Table 3. Comparison of B-Spline, VMC with B-Spline Prey Motion and Baseline Approaches (Case 1).

N	Baseline Solution PI	Baseline CPU(s)	B-Spline Solution PI	B-Spline CPU(s)	VMC Solution PI	VMC CPU(s)
8	91.8006	11.2	91.7534	1.2	91.7526	6.1
10	91.7317	16.9	91.7564	4.0	91.7410	6.4
12	91.7390	25.8	91.7503	3.4	91.7363	14.4
15	91.7315	55.8	91.7503	4.3	91.7456	16.2

Table 4 shows a similar comparison for case 2. Case 2 simulates a rest to rest rotation. The initial attitude represents a nadir attitude. The spacecraft is commanded to rotate to an attitude of 45 deg in each axis with body rates equal 0 deg/s in each axis. This simulates a situation where a CubeSat might be tasked to point at another object in orbit, such as for imaging or communication purposes.

Table 4. Comparison of B-Spline, VMC with B-Spline Prey Motion and Baseline Approaches (Case 2).

N	Baseline Solution PI	Baseline CPU(s)	B-Spline Solution PI	B-Spline CPU(s)	VMC Solution PI	VMC CPU(s)
8	3.69518	5.9	3.72487	3.1	3.7080	8.5
10	3.70767	13.2	3.70816	3.6	3.7057	12.6
12	3.69525	35.2	3.70813	4.0	3.7014	6.9
15	3.69507	47.1	3.70949	4.4	3.7001	12.3

From the average percent difference in performance index between the B-Spline and Baseline, and the average percent difference between the VMC with B-Spline prey motion and the baseline, it appears that both the B-Spline and VMC with B-Spline prey motion provide nearly equivalent solutions at reduced computational cost. The next set of figures gives a visual representation of the differences to illustrate that the B-Spline and VMC with B-Spline prey motion do provide nearly equivalent solutions. In Figure 13, the quaternion (with 10 LGL nodes), is plotted for the B-Spline (circle), VMC with B-Spline prey motion (+) and the baseline (line). It is easy to see that all three solutions meet the constraints and provide smooth rotations from the initial to final attitudes.

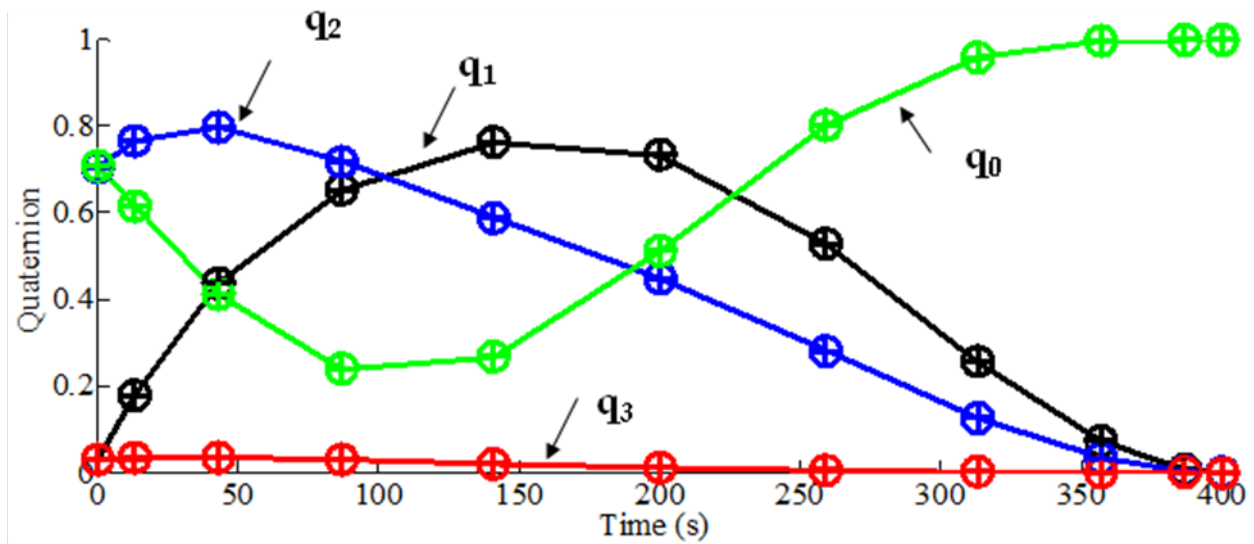


Figure 13. Quaternion of the near optimal attitude trajectory (Case 1)

Figure 14 shows a similar plot for body rates, also for Case 1. Again, the change is smooth and clearly meets the constraints given.

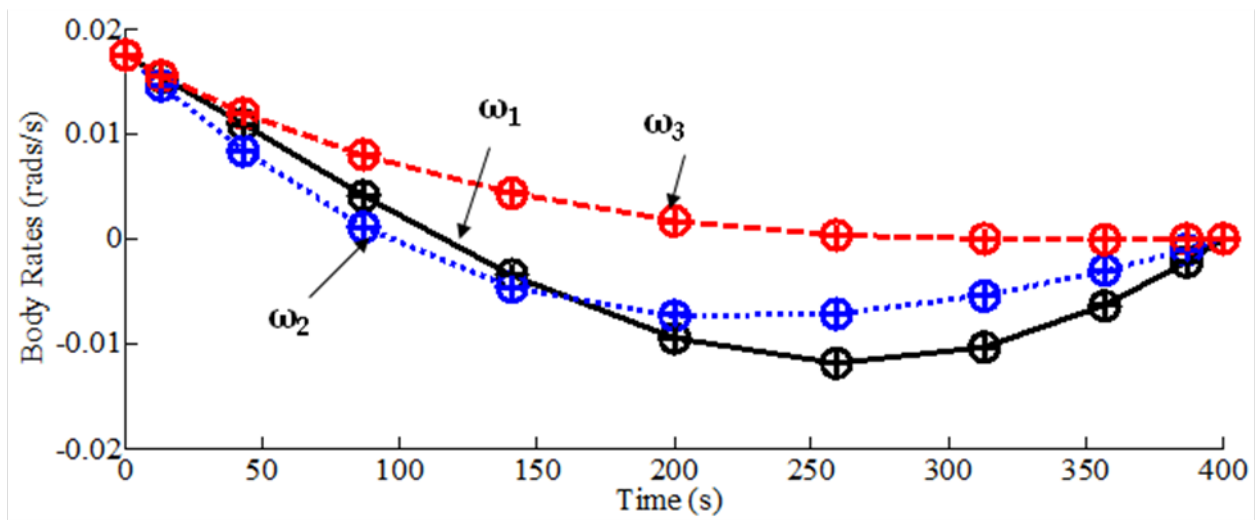


Figure 14. Angular velocity of the near optimal attitude trajectory.

Ultimately, the control command that comes from the flight computer in real hardware will change the current flowing through the coils. For this reason, Figure 15 is presented to show the change in current throughout the maneuver for the baseline, B-Spline and VMC with B-Spline prey motion methods. Again, each curve meets the constraints and is smooth enough for use in actual hardware.

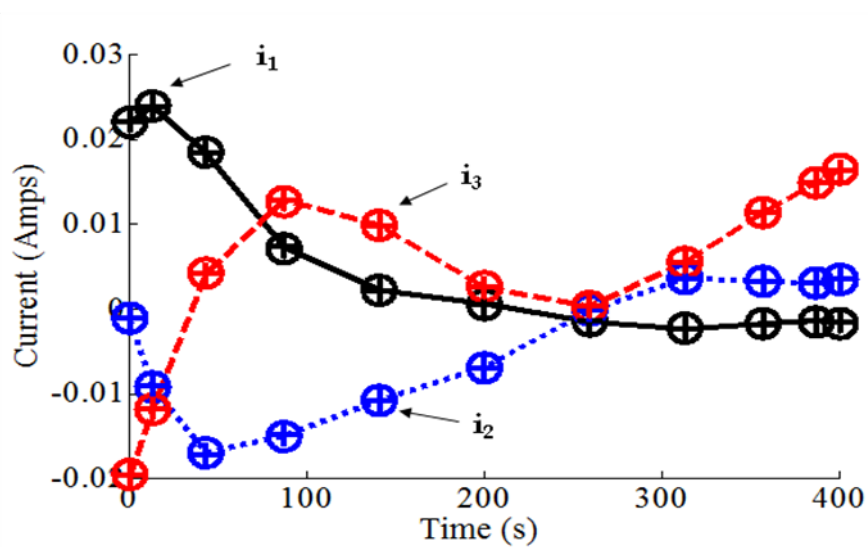


Figure 15. Current for near optimal rotation.



Figures 16-18 show the commanded torque for the baseline (line), B-Spline(circle) and VMC with B-Spline prey motion (+). The total torque is the solid black line, the Coil torque is the dashed blue line and the dotted red line represents the thruster torque. Clearly, the commanded torque obeys the constraint listed in the problem and is smooth enough for actual hardware.

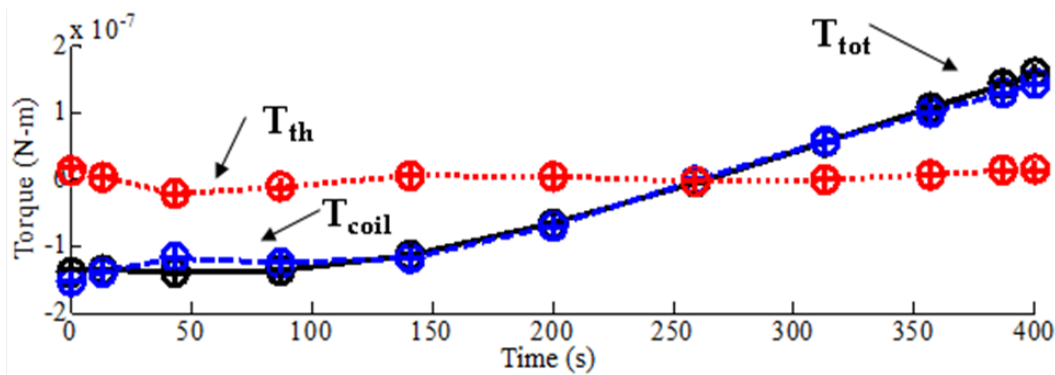


Figure 16. VMC control torque for near optimal rotation (X axis).

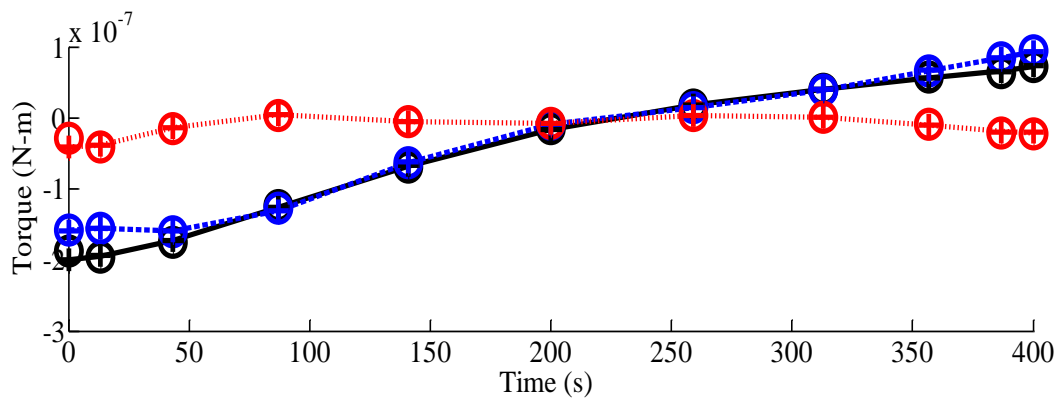


Figure 17. VMC control torque for near optimal rotation (Y axis).

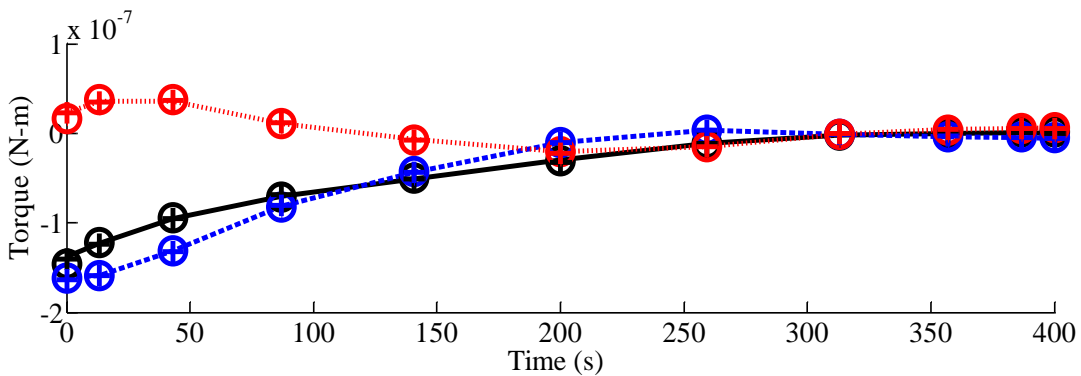


Figure 18. VMC control torque for near optimal rotation (Z axis).

Figures 19 and 20 illustrate the quaternion and body rates in case 2 (with 10 LGL nodes), for the B-Spline (circle), VMC with B-Spline prey motion (+) and the baseline (line). As before, all three solutions meet the constraints and provide smooth rotations from the initial to final attitudes.

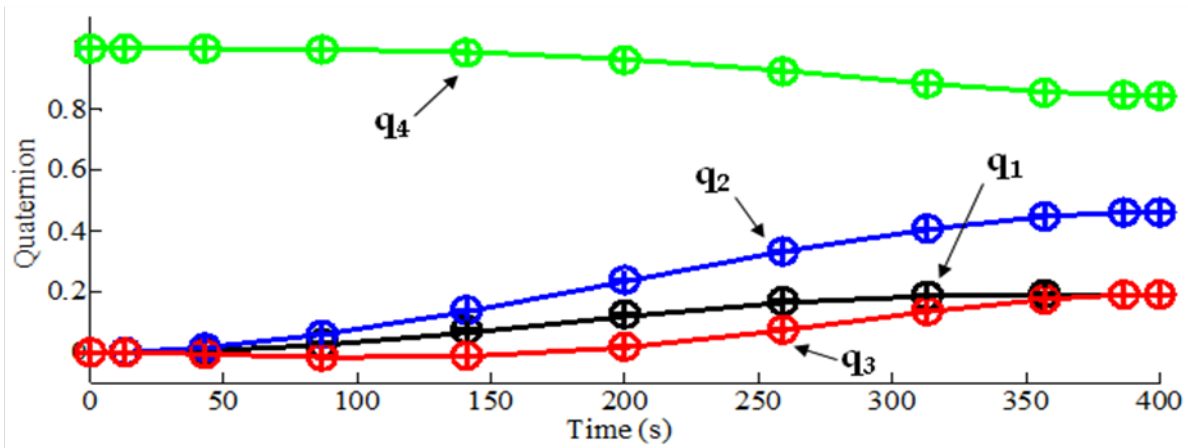


Figure 19. Quaternion for Case 2, B-Spline prey motion, 10 LGL Nodes,  $t_f=400s$ .

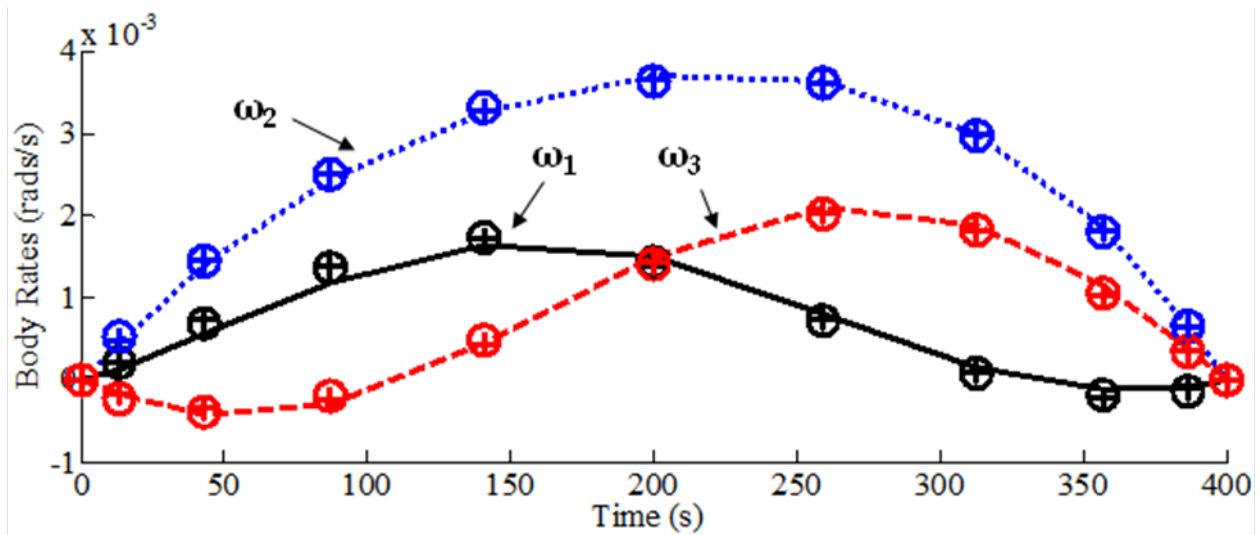


Figure 20. Angular velocity for Case 2, B-Spline prey motion, 10 LGL Nodes,  $t_f=400s$ .

Figure 21, which shows the plot of the current for each of the three methods, also demonstrates that it meets the constraints and is smooth enough for actual hardware.

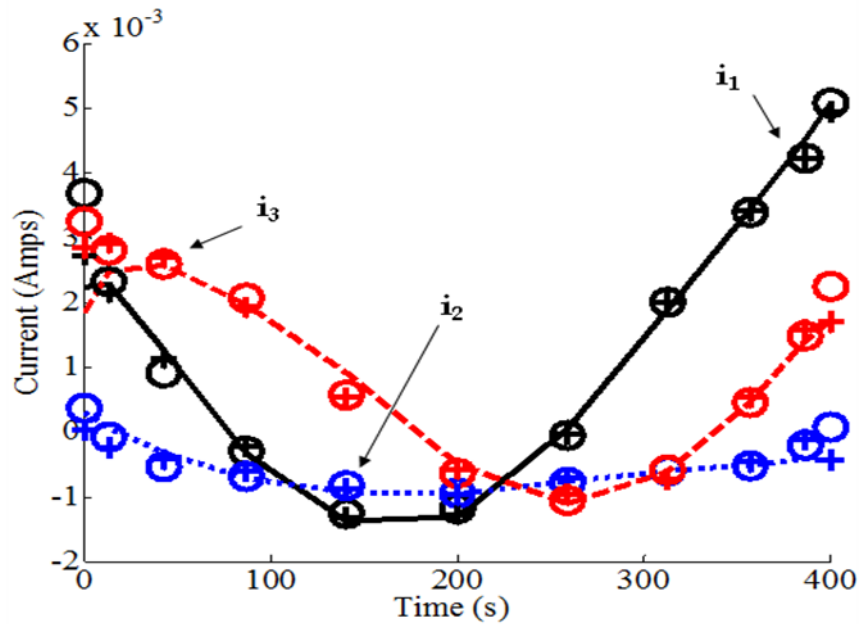


Figure 21. Current for Case 2, B-Spline prey motion, 10 LGL Nodes,  $t_f=400s$ .

Finally, the commanded torque for the baseline (line), B-Spline(circle) and VMC with B-Spline prey motion (+) are plotted in Figures 22-24. As before, the total torque is the solid black line, the coil torque is the dashed blue line and the dotted red line represents the thruster torque. Once more, the commanded torque obeys the constraint listed in the problem and is smooth enough for implementation in actual hardware.

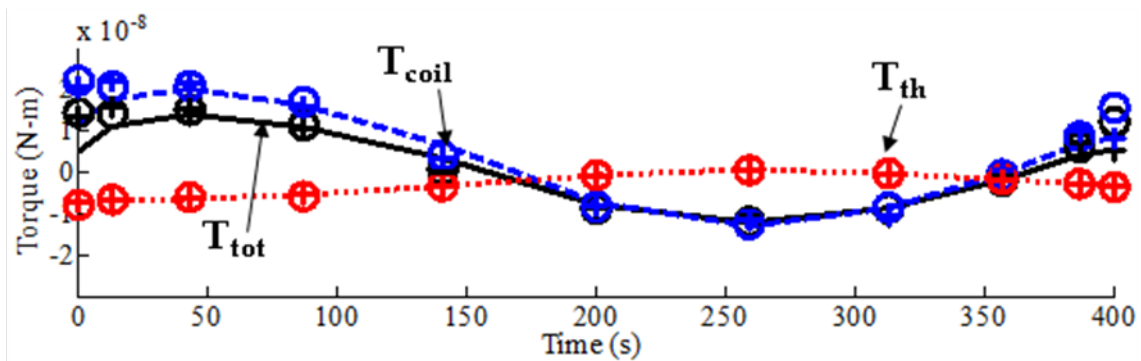


Figure 22. Torque (x-axis) for Case 2, B-Spline prey motion, 10 LGL Nodes,  $t_f=400s$ .

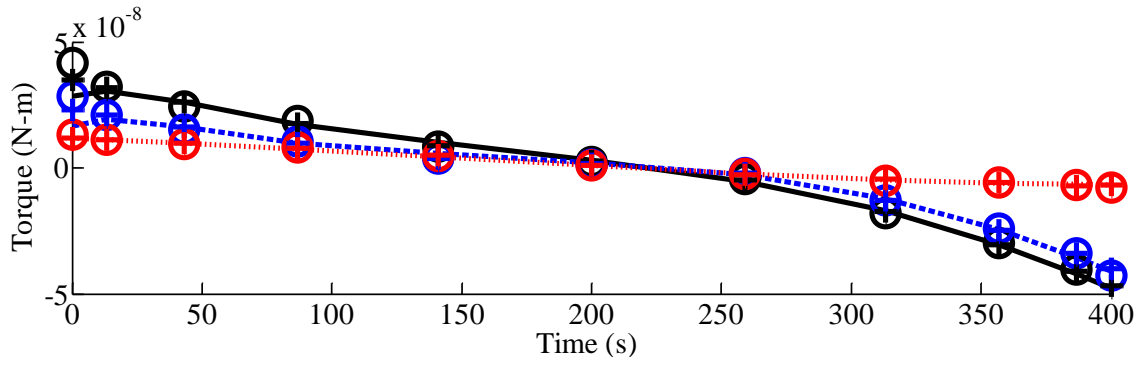


Figure 23. Torque (y-axis) for Case 2, B-Spline prey motion, 10 LGL Nodes,  $t_f=400$ s.

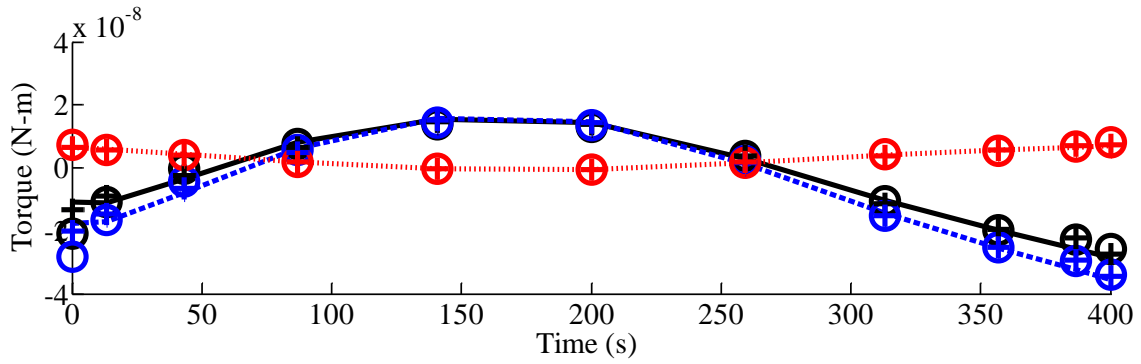


Figure 24. Torque (z-axis) for Case 2, B-Spline prey motion, 10 LGL Nodes,  $t_f=400$ s.

## CHAPTER 6: SUMMARY AND FUTURE WORK

In this thesis, four different methods were used to develop open loop optimal attitude control solutions that could be used as a reference trajectory for a feedback controller to track. These methods, the baseline, VMC with a polynomial prey motion, B-Spline, and VMC with a B-Spline prey motion were applied to two fuel optimal attitude control problems for a CubeSat: 1) minimizing the total torque for a given rotation and 2) minimizing the thruster torque in a system with combined thrusters and magnetic torque coils. The methods were then compared to the solutions generated by the baseline to determine the optimality of their solutions and the reduction in computational cost they could provide.

In general, both the B-Spline and the VMC augmented with the B-Spline prey motion methods have been shown to decrease the optimization time when compared to the baseline solution while the solution optimality is not sacrificed much. It has also been shown that the B-Spline method provides slightly faster solutions when providing the optimal attitude control management (problem 2) in situations *without* severe path constraints that prevent a less curved path between boundary points. Discussion was provided on why problems *with* path constraints would cause a greater (when compared to the VMC with a B-Spline prey motion method) increase in optimization parameters for the B-Spline method with an associated increase in computational cost. The result is that the VMC with B-Spline prey motion should provide results with a lower computational cost when severe path constraints exist.

For this reason, it is suggested that future work investigate the performance and utility of the VMC with a B-Spline prey motion method in realistic situations with significant path constraints. These realistic situations could also include known disturbances and the

incorporation of any additional constraints associated with the implementation in actual hardware. It is also suggested that some investigation of alternate parameterizations of the attitude representation be undertaken. Some possible candidates include the Rodriguez parameters and the Euler axis/angle parameterization (sometimes called the Rotation vector), both of which are ultimately based on four independent variables. Each of these has their own drawbacks (e.g. rotations limited to 180 degrees in the former, undefined values at zero for the latter), but they may offer opportunities to reduce the computational burden further, which seems to be significantly affected by the quaternion normalization constraint. These investigations may lead to even greater capability for the proposed VMC algorithm, proving yet another tool for providing near optimal solutions even faster than before.

## LIST OF REFERENCES

- [1] “CubeSat Design Specification, Version 12,” *California Polytechnic University*, URL: [http://cubesat.atl.calpoly.edu/images/developers/cds\\_rev12.pdf](http://cubesat.atl.calpoly.edu/images/developers/cds_rev12.pdf) [cited 25 August 2011].
- [2] “List of CubeSat Satellite Missions,” URL: <http://mtech.dk/thomsen/space/cubesat.php> [cited 25 August 2011].
- [3] “CubeSat mission listing,” URL: <http://www.cubesat.org/index.php/missions> [cited 25 August 2011].
- [4] “Aggiesat 2,” URL: [http://space.skyrocket.de/index\\_frame.htm?http://space.skyrocket.de/doc\\_sdat/aggiesat-2.htm](http://space.skyrocket.de/index_frame.htm?http://space.skyrocket.de/doc_sdat/aggiesat-2.htm) [cited 25 August 2011].
- [5] “BEESAT-1,” URL: <http://www.raumfahrttechnik.tu-berlin.de/beesat/v-menue2/beesat-1> [cited 25 August 2011].
- [6] “UWE-2,” URL: <http://directory.eoportal.org/presentations/13799/10001331.html> [cited 25 August 2011].
- [7] “AAUSAT II,” URL: <http://aausatii.space.aau.dk/homepage/index.php?language=en&page=adcs/adcs> [cited 25 August 2011].
- [8] Gregory, B., “Attitude Control System Design For Ion, The Illinois Observing Nanosatellite,” Master's Thesis, Marquette University, Milwaukee, WI, 2001.

- [9] Sarda, K., Grant, C., Eagleson, S., Kekez, D., and Zee, R., "Canadian Advanced Nanospace Experiment 2: On-Orbit Experiences with a Three-Kilogram Satellite," *Proceedings 22nd Annual AIAA/USU Conference on Small Satellites*, Logan, Utah, 2008.
- [10] Nielsen, J., Larsen, J., Sorensen, K., Grunnet, J., Kragelund, M., and Michelsen, A., "AAUSAT-II, a Danish Student Satellite," *Asia-Pacific Regional Space Agency Forum*, URL: [http://www.aprsaf.org/feature/feature\\_71.html](http://www.aprsaf.org/feature/feature_71.html) [cited 25 Aug 2011].
- [11] "The Texas Satellite Design Laboratory: An Overview of Our Current Projects," URL: [http://lightsey.ae.utexas.edu/publications/TEXAS\\_CubeSat\\_2011\\_Presentation.pdf](http://lightsey.ae.utexas.edu/publications/TEXAS_CubeSat_2011_Presentation.pdf) [cited 05 Nov 2011].
- [12] Martel, F., Pal, P., and Psiaki, M.L. "Active Magnetic Control System For Gravity Gradient Stabilized Spacecraft," *Proceedings Of The 2nd Annual AIAA/USU Conf. On Small Satellites*, Logan, Utah, 1988.
- [13] Musser, K.L., and Ward, L.E. "Autonomous Spacecraft Attitude Control Using Magnetic Torquing Only," *In Flight Mechanics Theory Symposium*. NASA. pp. 23-37.
- [14] Bak, T., Wisniewski, R., and Blanke, M. "Autonomous Attitude Determination And Control System For The Orsted Satellite," *1996 IEEE Aerospace Application Conference*. Vol 2, IEEE, Aspen, CO, 1996. pp. 173 - 186.
- [15] Wisniewski, R. "Linear Time Varying Approach To Satellite Attitude Control Using Only Electromagnetic Actuation," *Journal of Guidance, Control and Dynamics*, Vol. 23, No. 4, 2000, pp. 640-647.



- [16] Wisniewski R., and Blanke, M. "Three-axis Attitude Control Based on Magnetic Torquing," *Automatica*, Vol. 35, No. 7, 1999, pp. 1201-1214.
- [17] Makovec, K. "A Nonlinear Magnetic Controller For Three-Axis Stability Of Nanosatellites," Master's Thesis, Virginia Polytechnic Institute, Blacksburg, VA, 2001.
- [18] Fauske, K., "NCUBE Attitude Control," Master's Thesis, Norwegian University of Science and Technology (NTNU), Trondheim, Norway, 2003.
- [19] Gravdahl, J., "Magnetic Attitude Control For Satellites. " *43rd IEEE Conference On Decision And Control*, Atlantis, Paradise Island, Bahamas, 2004.
- [20] Liang, J., Fullmer, R., and Chen, Y., "Time-Optimal Magnetic Attitude Control For Small Spacecraft." *43rd IEEE Conference On Decision And Control*, Atlantis, Paradise Island, Bahamas, 2004.
- [21] Yan, H., Fleming, A., Ross, M., and Alfriend, K., "Real-Time Computation of Time Optimal Magnetic Attitude Control." AAS Paper 05-233, *2005 AAS/AIAA Space Flight Mechanics Conference*, Copper Mountain, CO, 2005.
- [22] Yan, H., Ross, M., and Alfriend, K., "Pseudospectral Feedback Control for Three-Axis Magnetic Attitude Stabilization in Elliptic Orbits," *Journal of Guidance, Control, and Dynamics*, Vol. 30, No. 4 , 2007, pp. 1107-1115.
- [23] Fahroo, F., and Ross, M. "Costate Estimation by a Legendre Pseudospectral Method," *Journal of Guidance, Control, and Dynamics*, Vol. 24, No. 2, 2001, pp. 270-277.

- [24] Fahroo, F., and Ross, M. "Pseudospectral Methods for Infinite-Horizon Nonlinear Optimal Control Problems," *Journal of Guidance, Control, and Dynamics*, Vol. 31, No. 4, 2008, pp. 927-936.
- [25] Bedrossian, N., Bhatt, S., Lammers, M., and Nguyen, L., "Zero Propellant Maneuver Flight Results for 180° ISS Rotation," *2007 International Symposium on Space Flight Dynamics*, NASA/CP-2007-214158, 2007.
- [26] Bhatt, S.A., "Optimal Reorientation of Spacecraft Using Only Control Moment Gyroscopes," Master's Thesis, Rice University, Houston, Texas, 2007.
- [27] Kang, W., and Bedrossian, N., "Pseudospectral Optimal Control Theory Makes Debut Flight, Saves NASA \$1M in Under Three Hours." *SIAM News*, Vol. 40, No. 7, 2007.
- [28] Zhou, Z., "Spacecraft Attitude Tracking and Maneuver Using Combined Magnetic Actuators." AIAA Paper 2010-7899, *AIAA Guidance, Navigation, and Control Conference*, Toronto, Ontario, 2010.
- [29] "VACCO ChEMS Micro-Propulsion System: Micro-Propulsion Overview," *VACCO Industries*, URL: <http://www.vacco.com/vacco/pdfs/mips2112.pdf> [cited 10 February 2010].
- [30] Vallado, D.A., *Fundamentals of Astrodynamics and Applications*, The McGraw-Hill Companies, Inc., New York, NY, 1997.
- [31] "Astrodynamics-Propagation Specifications, Technical Definitions, and Recommended Practices," ANSI/AIAA S-131-2010, 2010.
- [32] Wertz, J. R., *Spacecraft Attitude Dynamics and Control*, D. Reidel, Boston, 1978.

- [33] H.D. Curtis, *Orbital Mechanics For Engineering Students*, Elsevier Butterworth-Heinemann, Burlington, MA, 2005, pp. 330-337.
- [34] International Geomagnetic Reference Field, URL: <http://ngdc.noaa.gov/IAGA/vmod/igrf.html>. IGRF [cited 3 June 2010].
- [35] Xu, Y., "Subspace Optimal Control and Motion Camouflage," *AIAA Guidance, Navigation, and Control Conference and Exhibit*, Honolulu, HI, 2008.
- [36] Xu, Y., and Bassett, G., "Optimal Coherent Phantom Track Design using Virtual Motion Camouflage," *Proceedings of the American Control Conference*, Baltimore, MD, 2010.
- [37] Hesthaven, J., Gottlieb, S. and Gottlieb, D., *Spectral Methods for Time-Dependent Problems*, Cambridge University Press, Cambridge, UK, 2007, pp. 81-96.
- [38] Benson, D., Huntington, G., Thorvaldsen, T., and Rao, A., "Direct Trajectory Optimization and Costate Estimation via an Orthogonal Collocation Method," *Journal of Guidance, Control, and Dynamics, Engineering Notes*, Vol. 29, No. 6, 2006, pp. 1435-1440.
- [39] Piegl, L., and Tiller, W., *The NURBS Book*, Springer-Verlag, Berlin, Germany, 1997.
- [40] Chobotov, V. A., *Spacecraft Attitude Dynamics and Control*, Krieger Publishing Company, Malabar, 1991.
- [41] Sidi, M., *Spacecraft Dynamics and Control*, Cambridge University Press, Cambridge, UK, 2000, pp. 179-186.
- [42] Alberti, V., Assalone, A., Baldini, V., et al., "The AtmoCube project, an educational and scientific satellite at the University of Trieste," *1st IAA Conference on University Satellites Missions and CubeSat Workshop in Europe*, Roma, Italy, 2011.